

# **SANDIA REPORT**

SAND2018-7372  
Unlimited Release  
Printed June 2018

## **Verification and Validation of Simulation Framework for Analysis of Traumatic Brain Injury**

Paul A. Taylor, John S. Ludwigsen, Corey C. Ford, Andrei A. Vakhtin

Prepared by  
Sandia National Laboratories  
Albuquerque, New Mexico 87185 and Livermore, California 94550

This work funded through the U.S. Naval Health Research Center,  
Office of Naval Research, Mr. James Mackiewicz, Project Funding Manager.

Sandia National Laboratories is a multimission laboratory managed and operated  
by National Technology and Engineering Solutions of Sandia, LLC, a wholly owned  
subsidiary of Honeywell International, Inc., for the U.S. Department of Energy's  
National Nuclear Security Administration under contract DE-NA0003525.



**Sandia National Laboratories**

Issued by Sandia National Laboratories, operated for the United States Department of Energy by National Technology and Engineering Solutions of Sandia, LLC.

**NOTICE:** This report was prepared as an account of work sponsored by an agency of the United States Government. Neither the United States Government, nor any agency thereof, nor any of their employees, nor any of their contractors, subcontractors, or their employees, make any warranty, express or implied, or assume any legal liability or responsibility for the accuracy, completeness, or usefulness of any information, apparatus, product, or process disclosed, or represent that its use would not infringe privately owned rights. Reference herein to any specific commercial product, process, or service by trade name, trademark, manufacturer, or otherwise, does not necessarily constitute or imply its endorsement, recommendation, or favoring by the United States Government, any agency thereof, or any of their contractors or subcontractors. The views and opinions expressed herein do not necessarily state or reflect those of the United States Government, any agency thereof, or any of their contractors.

Printed in the United States of America. This report has been reproduced directly from the best available copy.

Available to DOE and DOE contractors from  
U.S. Department of Energy  
Office of Scientific and Technical Information  
P.O. Box 62  
Oak Ridge, TN 37831

Telephone: (865) 576-8401  
Facsimile: (865) 576-5728  
E-Mail: [reports@osti.gov](mailto:reports@osti.gov)  
Online ordering: <http://www.osti.gov/scitech>

Available to the public from  
U.S. Department of Commerce  
National Technical Information Service  
5301 Shawnee Rd  
Alexandria, VA 22312

Telephone: (800) 553-6847  
Facsimile: (703) 605-6900  
E-Mail: [orders@ntis.gov](mailto:orders@ntis.gov)  
Online order: <https://classic.ntis.gov/help/order-methods/>



SAND2018-7372  
Printed June 2018  
Unlimited Release

# **Verification and Validation of Simulation Framework for Analysis of Traumatic Brain Injury**

Paul A. Taylor  
John S. Ludwigsen  
Terminal Ballistics Department, 5421  
Sandia National Laboratories  
Albuquerque, New Mexico 87185

Corey C. Ford  
Andrei A. Vakhtin  
Department of Neurology  
University of New Mexico Health Sciences Center  
Albuquerque, NM 87131-0001

## **Abstract**

Many U.S. troops deployed in Iraq and Afghanistan have suffered blast-related, closed-head injuries as a result of being within non-lethal distance of a detonated improvised explosive device (IED). Consequently, we are conducting a modeling & simulation investigation, coupled with clinical diagnostics of brain injury, into the mechanisms associated with blast to the human head that give rise to traumatic brain injury (TBI). In particular, we are attempting to identify the specific conditions of focused stress wave energy within the brain, resulting from blast loading to the head, which define a threshold for persistent brain injury. As these threshold injury conditions are identified, one can then employ a modeling & simulation toolset to assess the efficacy of various helmet designs to mitigate blast exposure that would otherwise lead to traumatic brain injury. In this report, we describe our efforts to establish the role of stress wave interactions in the genesis of traumatic brain injury (TBI) from exposure to explosive blast. We discuss our effort to correlate simulation predictions with clinical assessments of TBI subjects whose brain injuries have been diagnosed by advanced magnetic resonance imaging techniques. This work has been funded through the U.S. Naval Health Research Center, Office of Naval Research, Mr. James Mackiewicz, project funding manager.

## **ACKNOWLEDGMENTS**

This work funded through the U.S. Naval Health Research Center, Office of Naval Research, Mr. James Mackiewicz, project funding manager.

The authors acknowledge the National Library of Medicine and the Visible Human Project as the source of the Visible Human Data Set used to construct the digital head/neck models employed in this research.

The authors are indebted to Professor Philip Bayly and his research team at Washington University, St. Louis MO, in providing magnetic resonance tagging data with which to validate our models and permission to use this data and the images. Figures in this report that are reproduction of the Bayly team original figures are indicated in the figure caption.

The authors thank Dr. Chad Hovey and Mr. Douglas Dederman for their review and editing of the original version of this report, SAND2012-8705, Investigation of Blast-Induced Traumatic Brain Injury and its Mitigation, OOU/ECI/Distribution C, to create the current document in unclassified, unlimited release form.

Sandia National Laboratories is a multimission laboratory managed and operated by National Technology & Engineering Solutions of Sandia, LLC, a wholly owned subsidiary of Honeywell International Inc., for the United States Department of Energy's National Nuclear Security Administration under contract DE-NA0003525.

## TABLE OF CONTENTS

1	Introduction.....	13
2	Modeling and Simulation Methodology .....	15
	2.1 Head/Neck Model .....	15
	2.1.1 Geometric Representation.....	15
	2.1.2 Constitutive Models .....	16
	2.2 Simulation Codes .....	19
3	Modeling Validation .....	21
	3.1 Simulation of Magnetic Resonance Image Tagging Experiments.....	21
	3.1.1 Head Rotation Experiment.....	21
	3.1.2 Forehead Impact Test.....	26
	3.2 Simulation of APL Field Blast Data .....	32
	3.2.1 Simulation Results .....	34
4	Blast Simulations of Unprotected Head.....	39
	4.1 Stress Wave Magnitude versus Energy.....	39
	4.2 Influence of Blast Direction.....	41
	4.3 Spatial Variance of Energy Deposition.....	46
5	Concluding Remarks.....	47
	References .....	49
	DISTRIBUTION.....	53

## FIGURES

Figure 1. Finite volume version of head/neck model in various positions and cutaway sections. Top: front, rear, and left side views. Bottom: coronal, axial, and mid-sagittal cuts showing internal structure. ....	15
Figure 2. Finite element version of head/neck model in various cutaway sections. Left to right: coronal, axial, and mid-sagittal cuts showing internal structure of the model.....	16
Figure 3. Adiabatic compression curve for dry air generated by our tabular EOS representation. ....	18
Figure 4. Initial condition, prior to the twisting movement of the head. The black dot is the rotation stopper. (Reprinted with permission from the author).....	21
Figure 5. Initial-to-final configuration showing twisting movement of the head and the harness hitting the stopping mechanism. (Reprinted with permission from the author).....	22
Figure 6. Typical angular rotation history imposed on the head in simulations of the Bayly experiments. ....	22
Figure 7. Finite element head/neck model used in head rotation analysis. Sinus air and scalp/muscle has been removed from the model for this analysis. ....	23
Figure 8. Location of the planes used in the experiments. (Reprinted with permission from the author). ....	24
Figure 9. Calculated shear strains from PRESTO simulation at selected times on the “+2 cm” plane. The 38 ms time, indicated in a red box, was used as a specific comparison to the Bayly experimental results. ....	25

Figure 10. Calculated shear strains at selected times from Bayly’s head rotation experiment. (Reprinted with permission from the author). The 228 ms time, indicated in a red box, was used as a specific comparison to the PRESTO simulation results. ....	26
Figure 11. Direction of head travel. Image (a) displays the mid-sagittal plane. (Reprinted with permission from the author). ....	27
Figure 12. Rigid-body motion of the skull versus time. (Reprinted with permission from the author). ....	27
Figure 13. The four sites in the brain where displacement and strain were calculated in the impact experiments. (Reprinted with permission from the author).....	28
Figure 14. Measured displacement at four locations for three different test subjects. (Reprinted with permission from the author). ....	29
Figure 15. Simulation predictions of relative displacement at four locations (a-d) in the brain. .	30
Figure 16. Calculated displacements relative to the skull for three test subjects. (Reprinted with permission from the author). ....	31
Figure 17. Stop-action plots of blast-induced pressure waves propagating through the head from the front (left), rear (center), and lateral (right) directions. ....	32
Figure 18. Pressure pulse generated by a 1.3 MPa (13 bars) of blast wave.....	32
Figure 19. Test configuration of the APL field test blast experiments on their Human Surrogate Head Model (HSHM). ....	33
Figure 20. Pressure pulse of 0.36 MPa (360 KPa) magnitude generated in APL blast experiments on their Human Surrogate Head Model (HSHM). ....	33
Figure 21. Diagram of sensor placement in the APL Human Surrogate Head Model (HSHM)..	34
Figure 22. Time-lapse images of frontal blast exposure showing pressure in the mid-sagittal plane of the head/neck model. Upper pressure limit is 500 KPa. Regions without color are at or below the threshold pressure of 1 atmosphere (100 KPa). ....	35
Figure 23. Time-lapse images of frontal blast exposure showing pressure in an axial plane just about the orbits of the head/neck model. Upper pressure limit is 500 KPa. Regions without color are at or below the threshold pressure of 1 atmosphere (100 KPa). .	35
Figure 24. Time-lapse images of frontal blast exposure showing effective (shear) stress levels in the mid-sagittal plane of the head/neck model. ....	36
Figure 25. Time-lapse images of frontal blast exposure showing effective (shear) stress levels in an axial plane just about the orbits (eye sockets) of the head/neck model.....	36
Figure 26. Comparison of simulation predictions with the APL blast test pressure data taken from their Human Surrogate Head Model (HSHM) for a 3.6 bar (360 KPa) frontal blast. ....	37
Figure 27. Plots of maximum stress and energy in the mid-sagittal plane for a 360 KPa frontal blast. (a) Maximum compressive pressure (blue: 0.1 MPa; red: 1 MPa) and (b) corresponding isotropic compressive energy (blue: 1 J/m <sup>3</sup> ; red: 300 J/m <sup>3</sup> ). (c) Maximum tensile pressure (blue: 1 KPa; red: 200 KPa) and (d) corresponding isotropic tensile energy (blue: 1 J/m <sup>3</sup> ; red: 200 J/m <sup>3</sup> ). (e) Maximum deviatoric (shear) stress (blue: 0.1 KPa; red: 20 KPa) and (f) corresponding shear strain energy (blue: 1 J/m <sup>3</sup> ; red: 300 J/m <sup>3</sup> ). Plot variable levels increase from blue (minimum), green, yellow, and red (maximum). Black denotes that the plot variable max limit has been exceeded.....	40
Figure 28. Plots of maximum Isotropic Compressive Energy in various anatomical planes for a 360 KPa blast. Top row: Frontal blast, mid-sagittal and axial planes; middle row:	

	rear blast; bottom row: right side blast, mid-coronal and axial planes. Color scale: blue: 1 J/m <sup>3</sup> ; red: 300 J/m <sup>3</sup> , black denotes that the plot variable maximum limit has been exceeded. Positive energies are associated with compressive loading. ....	43
Figure 29.	Plots of maximum Isotropic Tensile Energy in various anatomical planes for a 360 KPa blast. Top row: Frontal blast, mid-sagittal and axial planes; middle row: rear blast; bottom row: right side blast, mid-coronal and axial planes. Color scale: blue: 1 J/m <sup>3</sup> ; red: 200 J/m <sup>3</sup> ; black denotes that the plot variable maximum limit has been exceeded. Negative energies are associated with tensile loading. ....	44
Figure 30.	Plots of maximum Deviatoric (Shear) Energy in various anatomical planes for a 360 KPa blast. Top row: Frontal blast, mid-sagittal and axial planes; middle row: rear blast; bottom row: right side blast, mid-coronal and axial planes. Color scale: blue: 1 J/m <sup>3</sup> ; red: 300 J/m <sup>3</sup> , black denotes that the plot variable maximum limit has been exceeded. Deviatoric energy is always positive. ....	45

## TABLES

Table 1.	Elastic and fracture material properties of head/neck model. ....	17
Table 2.	Viscoelastic material properties of brain tissue. ....	18

**INTENTIONALLY LEFT BLANK**

## EXECUTIVE SUMMARY

Many U.S. troops deployed in Iraq and Afghanistan have suffered blast-related, closed-head injuries as a result of being within non-lethal distance of a detonated improvised explosive device (IED). Consequently, we are conducting a modeling and simulation investigation, coupled with clinical diagnostics of brain injury, into the mechanisms associated with blast to the human head that give rise to traumatic brain injury (TBI). In particular, we are attempting to identify the specific conditions of focused stress wave energy within the brain, resulting from blast loading to the head, which define a threshold for persistent brain injury.

As these threshold injury conditions are identified, one can then employ a modeling and simulation toolset to assess the efficacy of various helmet designs to mitigate blast exposure that would otherwise lead to brain injury. In this report, we describe our efforts to establish the role of stress wave interactions in the genesis of TBI from exposure to explosive blast. This includes our efforts to correlate simulation predictions with clinical assessments of TBI subjects whose brain injuries have been diagnosed by advanced magnetic resonance imaging techniques.

This report is organized as follows:

Chapter 1 introduces and motivates the use of a modeling and simulation (M&S) framework to study TBI.

Chapter 2 describes our M&S methodology as well as the head/neck model we have developed for the study. The three main areas of this M&S framework are geometry, materials, and solvers. Geometry will describe the human anatomy model, reconstructed from medical imaging techniques. Materials will encompass the constitutive models used to describe response within a geometric entity. Finally, solvers will describe the simulation codes and platforms used to undertake simulations.

In Chapter 3, we successfully validate our constitutive models and simulation methods against independent experiments employing magnetic resonance tagging methods to measure brain displacements resulting from impulsive loading to the heads of live human subjects. For further validation, we also compare our simulation predictions of intracranial pressure histories to those measured in separate field test experiments in which a physical human head surrogate model is exposed to explosive blast.

In Chapter 4, we discuss the merits of predicting wave energy deposition in the brain as a suitable physics variable with which to correlate against clinically-measured brain damage. Chapter 4 then reports on our simulation results of blast exposure of the unprotected head.

In Chapter 5, we provide concluding remarks, including our accomplishments and outlook for future research directions.

Our simulations predict that the most damaging components of wave energy experience by the brain during blast exposure are independent of blast direction. This result, when verified, will be of great significance to helmet designers. However, in absence of a brain injury threshold criterion, the only way one can assess helmet protection from blast exposure is by means of a

relative merit assessment. In this regard, the following question arises: are the wave energy magnitudes experienced by the brain of an unprotected individual reduced by helmet protection and, if so, by how much?

We feel that the body of work presented in this report clearly demonstrates the merit of using a modeling and simulation approach to investigate the intricacies of brain injury resulting from impulsive loading to the head and neck. Starting in fiscal year 2013, we will use laboratory directed research and development (LDRD) funds to extend this capability by developing a full head/neck/torso model and the related methodology to simulate the injury mechanics associated with blast loading, blunt force impact, and ballistic projectile penetration.

This new M&S capability will allow us to investigate various armor strategies that mitigate injury to life-critical organs in the torso, neck, and head including the cardiovascular system, lungs, liver, spine, spinal cord, and brain. Once in place, we expect this capability to attract new partnership opportunities within the defense community who are interested in high fidelity investigations of wound ballistics and the development of advanced armor to protect our warfighters.

## NOMENCLATURE

### Engineering Terms

ACH – (U.S. Army) Advanced Combat Helmet

CTH – Eulerian shock wave physics wave computer code (not an acronym)

IED – Improvised Explosive Device

### Clinical/Medical Terms

ACC – Anterior Cingulate Cortex

BDI-II – Beck Depression Inventory II

BOLD – Blood Oxygenation Level Dependent

CSF – Cerebral Spinal Fluid

CT – Computed Tomography

COWAT – Controlled Oral Word Association Test

CVLT-II – California Verbal Learning Test II

Deafferentation – loss of neuronal connections to the white matter in brain

DAI – Diffuse Axonal Injury

DLPFC – Dorsal Lateral Prefrontal Cortex

DTI – Diffusion Tensor Image (or Imaging)

DWI – Diffusion Weighted Image (or Imaging)

EPI – Echo Planar Imaging

FNC – Functional Network Connectivity

fMRI – functional Magnetic Resonance Image (or Imaging)

GIFT – Group ICA fMRI Toolbox

GICA – Group Independent Component Analysis

IC(s) – Independent Component(s)

ICA – Independent Component Analysis

LOC – Loss of Consciousness

MANCOVAN – Multivariate Analysis of Covariance

MEG – Magnetoencephalography (or Magnetoencephalographic)

MFG – Middle Frontal Gyrus  
MNI -- Montreal Neurological Institute  
MR – Magnetic Resonance  
MRI – Magnetic Resonance Image (or Imaging)  
MTL – Medial Temporal Lobe  
NSI – Neurobehavioral Symptom Inventory  
OFC – Orbital Frontal Cortex  
PASAT – Paced Auditory Serial Addition Test  
PC(s) – Principal Component(s)  
PCS – Post Concussive Syndrome  
PTJ – Parietal-Temporal Junction  
PTSD – Post Traumatic Stress Disorder  
RSN – Resting State Network  
SD – Standard Deviation  
SLF – Superior Longitudinal Fasciculus  
TBI – Traumatic Brain Injury  
TE – Echo Time (MRI)  
TR – Repetition Time (MRI)  
VAMC – Veterans Administration Medical Center  
VLPFC – Ventrolateral Prefrontal Cortex  
WCST – Wisconsin Card Sorting Test  
WTAR – Wechsler Test of Adult Reading

## 1 INTRODUCTION

The annual incidence of traumatic brain injury (TBI) in the United States has been estimated at 1.4 million, accounting for one third of all injury related deaths [1]. As a result of the wars in Iraq and Afghanistan, the incidence of head injuries in the US armed forces has been on the rise. While US troops deployed in Iraq and Afghanistan today wear some of the most advanced armor in the world, improving their survivability dramatically, the rates of other non-fatal, yet debilitating, injuries have inevitably risen [2].

Recent combat statistics report that over 160,000 US soldiers deployed in Iraq and Afghanistan have sustained traumatic brain injury (TBI), with over 37,000 of those categorized at the moderate-to-severe level [3]. Furthermore, a significant number of those injuries were a result of blast. In fact, reports indicate that 69% of the soldiers returning from theatre and screening positive for TBI were caused by blast [4,5]. The principal source of these blast-induced brain injuries was one or more encounters with the blast wave produced by a detonated improvised explosive device (IED).

Injuries sustained from blast exposure have been categorized into three major types, primary, secondary, and tertiary [6]. Primary blast injury is associated with direct exposure of the head and body to the blast wave. In secondary blast injury, debris is accelerated into the individual, while in tertiary blast injury the victim is thrown into stationary objects by the blast. The role of primary blast exposure in the development of TBI is not well understood and is the focus of this work.

Modeling and simulation-based investigations into the causal relationship between explosive blast and TBI have recently begun to appear in the literature [7–9] in response to blast-related injuries experienced by U.S. military personnel in the Iraq and Afghanistan wars. These studies were based on partial models of the head that principally consists of the cranium and its contents without including the jaw and neck structures. The studies demonstrated the usefulness of employing a modeling and simulation approach in the investigation of blast-induced brain injuries. In our earlier study [8], we identified the significance of the early-time intracranial wave physics in the development of TBI that occur well before any ensuing head accelerations or rotations. However, these studies also revealed the need for refinement and completion of the virtual head models; specifically, the addition of the jaw and neck structures. To be useful as a tool to investigate the effectiveness of helmet design in blast protection, studies employing helmet models in virtual blast scenarios must also be undertaken. Some work has already been reported in this area [10–12]. Specifically, these studies focused on the blast mitigation effectiveness of helmet designs based on the Army Advanced Combat Helmet (ACH).

The remainder of this paper is organized as follows. Chapter 2 describes our modeling and simulation methodology as well as the head/neck and helmet models we have developed for the study. In Chapter 3, we report on our efforts to validate the constitutive models and simulation methods employed for the project. Chapter 4 presents blast simulations of the unprotected head. Chapter 5 contains concluding remarks.

**INTENTIONALLY LEFT BLANK**

## 2 MODELING AND SIMULATION METHODOLOGY

### 2.1 Head/Neck Model

#### 2.1.1 Geometric Representation

We have constructed a head/neck model based on the National Library of Medicine's Visible Human dataset [13] using 256 anatomical axial slices, 1mm-thick, of the human male starting from the base of the neck to the top of the head. The model possesses anatomically correct distributions of bone, white and gray brain matter, membranes (falx and tentorium), cerebral spinal fluid (CSF), and muscle/scalp (see Figure 1).

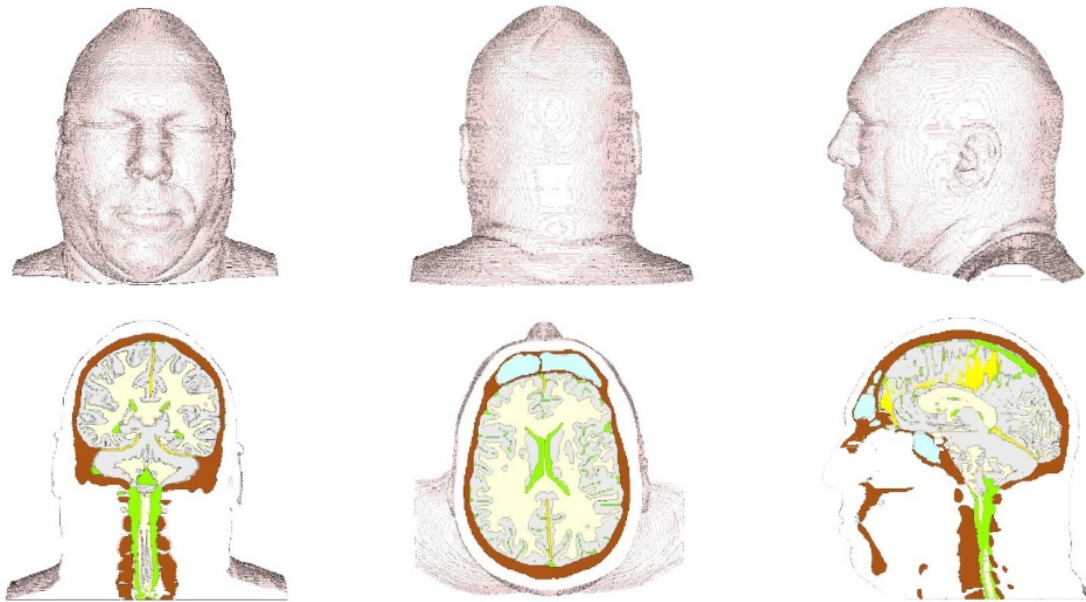


*Figure 1. Finite volume version of head/neck model in various positions and cutaway sections. Top: front, rear, and left side views. Bottom: coronal, axial, and mid-sagittal cuts showing internal structure.*

The head/neck model exists in both finite volume and finite element versions. The finite volume representation has been built specifically for import into the wave physics code CTH. The finite element version can be imported into any Lagrangian or coupled Lagrangian-Eulerian wave code. However, to simulate blast loading, the wave code must be capable of treating fluid-solid interactions.

The head/neck model consists of roughly 5.9 million cubic elements, each with a volume of one cubic millimeter. Although the model represents a 95th percentile male, the model's brain volume is typical of a 50th percentile individual. Specifically, the brain model possesses a volume of 1.41 liters. Selected cutaway views of the finite element version of the head/neck model appear in Figure 2.

Material properties of the head/neck model include those for (1) bone, (2) gray matter, (3) white matter, (4) membranes, (5) cerebral spinal fluid, and (6) muscle/scalp. These properties are

incorporated into a set of constitutive models that represent the dynamic mechanical response for each material. The constitutive models are described in Subsection 2.1.2.

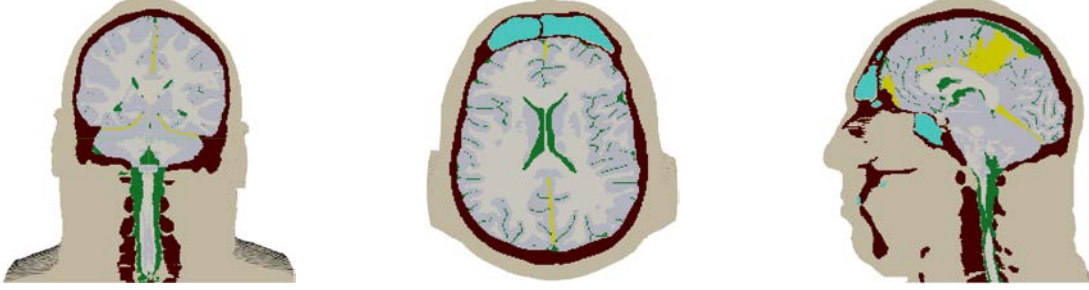


Figure 2. Finite element version of head/neck model in various cutaway sections. Left to right: coronal, axial, and mid-sagittal cuts showing internal structure of the model.

### 2.1.2 Constitutive Models

Our simulation method employs various equation-of-state (EOS) and constitutive models representing the six constituents of the head/neck model and the surrounding air. In this section, we describe the models used in the head/neck model and the surrounding air.

The bone material is represented by a compressible, linear elastic perfectly plastic strength model and an accumulated strain-to-failure fracture model, fit to material properties data reported by Zhang et al. [14] and Carter [15] for cortical bone. The models describing the volumetric and shear response of the skull are commonly understood and should require no further explanation. However, the failure model warrants further description where, in particular, we employed a strain-to-failure fracture model. This model introduces a damage variable  $D$  that is defined according to the relation

$$D(\mathbf{x}, t) = \int_0^t \frac{d\varepsilon^P}{\varepsilon_f^P}, \quad (1)$$

where  $\varepsilon^P$  is the equivalent plastic strain, continuously updated at each time step, and  $\varepsilon_f^P$  denotes the critical value of equivalent plastic strain at fracture.  $D = 0$  denotes undamaged material whereas failure is considered to have occurred whenever  $D$  reaches the value of 1. The damage variable is calculated for each material point in the skull at every time step, degrading both the plastic yield strength  $Y$  and fracture stress  $\sigma_f$  of the material in the following manner:

$$Y(\mathbf{x}, t) = Y_0[1 - D(\mathbf{x}, t)] \text{ and } \sigma_f(\mathbf{x}, t) = \sigma_f^0[1 - D(\mathbf{x}, t)], \quad (2)$$

where  $Y_0$  and  $\sigma_f^0$  denote values of yield and fracture stress, respectively, for undamaged material. For the skull material properties, we have selected data reported by Carter [15] in which  $Y_0 = 95$  MPa,  $\sigma_f^0 = 77.5$  MPa, and  $\varepsilon_f^P = 0.008$ . The equivalent plastic failure strain was determined from Carter's data which showed a total failure strain of 0.016 (elastic plus plastic components) and a yield strain of 0.008. The plastic strain at failure is determined to be the difference between the two. The complete list of material property values for the skull is listed in Table 1.

The white and gray brain matter are considered compressible, viscoelastic materials and assigned model representations similar to those proposed by Zhang et al. [14]. These two materials are represented by distinct, compressible elastic equation-of-state models for the volumetric response and by separate 3-term Maxwell viscoelastic models for their respective deviatoric (shear) response. The time-dependent shear modulus of these brain tissues is represented by the equation

$$G(t) = G_{\infty} + (G_0 - G_{\infty})e^{-\beta \cdot t}, \quad (3)$$

where  $t$  denotes time,  $G_0$  is the short-term shear modulus,  $G_{\infty}$  is the long-term modulus, and  $\beta$  denotes a viscous decay constant for the material. As reported by Zhang et al. [14], the form for the shear modulus function and its parameters were determined based on *in vitro* data obtained from vibration tests of the human brain [16]. The values of density and bulk moduli for these brain tissues in the current study were also taken from those specified by Zhang et al. [14] as being the most accurate. However, the viscoelastic decay constants for the white and gray matter turned out to be too large when we attempted to match the validation data of Bayly [17,18]. Consequently, we decreased  $\beta$  for these materials from 700/sec to 40/sec in order to provide the best match to that data. This point will be taken up further in Section 3.1 on model validation. The viscoelastic properties for the white and gray matter are listed in Table 2.

Table 1. Elastic and fracture material properties of head/neck model.

Material	Density (g/cc)	Bulk Modulus (MPa)	Shear Modulus (MPa)	Young's Modulus (MPa)	Poisson Ratio	Yield Stress (MPa)	Strain to Failure (%)	Fracture Stress (MPa)
Skull	1.21	4762	3279	8000	0.22	95	0.8	77.5
White Matter	1.04	2371	Table 2		0.49	--	--	--
Gray Matter	1.04	2371	Table 2		0.49	--	--	--
Falx & Tentorium	1.133	105	10.86	31.5	0.45	--	--	--
CSF	0.9998	1960	--		--	--	--	--
Muscle & Scalp	1.20	34.8	5.88	16.7	0.42	--	--	--
Dry Air	1.218e-3	Figure 2	--		--	--	--	--

The falx and tentorium membranes which partition the brain, as well as the scalp/muscle tissue are represented by compressible elastic models employing the material properties reported in [14]. These properties are listed in Table 1.

Table 2. Viscoelastic material properties of brain tissue.

	Short-term Shear Modulus $G_o$ (KPa)	Long-term Shear Modulus $G_\infty$ (KPa)	Decay Constant $\beta$ (sec <sup>-1</sup> )
White Matter	41.0	7.8	40
Gray Matter	34.0	6.4	40

In order to simulate blast, air must be represented in our simulations. Air envelops the head/neck models at ambient conditions, occupies the nasal sinuses, and transmits the blast wave. We have employed a non-linear, tabular equation-of-state representation for a dry air mix of N<sub>2</sub> (78.09%), O<sub>2</sub> (21.95%), and Ar (0.96%), reference density of 1.218e-3 g/cc, specifically designed for shock wave simulations [19]. The adiabatic compressibility of our air model is depicted graphically in Figure 3.

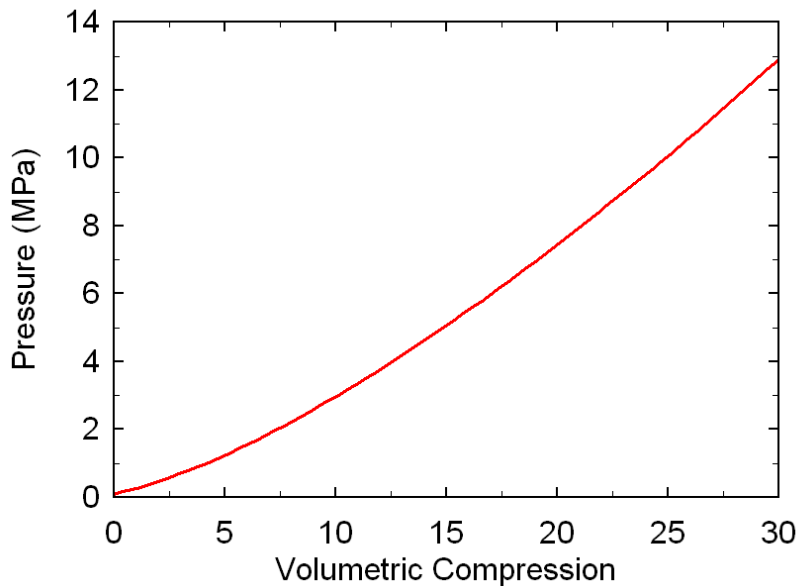


Figure 3. Adiabatic compression curve for dry air generated by our tabular EOS representation.

We have selected biological material models based on their accuracy and relevance to the problem at hand. Whenever possible, we have chosen models that have been validated against head impact data provided by Nahum et al. [20] and Feng [18]. Furthermore, we have made an attempt to validate our material models against conditions similar to those of interest here, i.e., the exposure of the human head and neck to an air blast. In particular, we have performed a consistency check of our models and simulation methodology by comparing our predictions with laboratory blast data on the physical head model developed at the Johns Hopkins Applied Physics Laboratory [21]. The details of this validation exercise are presented in Chapter 3.

## 2.2 Simulation Codes

We employ two simulation methods, each chosen for its relevance to the problem at hand. The blast simulations are performed using the shock wave physics code CTH [23]. CTH is an Eulerian finite-volume computer simulation code that is capable of tracking 20+ materials simultaneously, simulating their interactions as they undergo impact, blast loading, and penetration. This code adequately captures the fluid-solid interactions that occur between the pressurized air and the solid models for the head/neck and helmet.

To validate our head/neck model, we employed the transient dynamics code PRESTO [24] to simulate the magnetic resonance tagging experiments of Bayly et al. [17,18]. PRESTO is a Lagrangian finite element transient dynamics code more appropriate to simulating solid-solid interactions as well as material behavior in response to time-dependent kinematic boundary conditions.

Both CTH and PRESTO possess an extensive array of constitutive models that permit us to represent the biological tissue and ambient/pressurized air used in our simulations.

The specific initial and boundary conditions employed to duplicate the magnetic resonance tagging experiments of Bayly and the blast loading simulations with CTH will be discussed at length in the next chapter.

**INTENTIONALLY LEFT BLANK**

### 3 MODELING VALIDATION

#### 3.1 Simulation of Magnetic Resonance Image Tagging Experiments

A problem with modeling human head response including the brain tissue to either blast or impact loads is that the material properties of living brain tissue are not well characterized. Recent work, of Feng, et al. [18] at Washington University in St. Louis, has employed magnetic resonance image (MRI) tagging techniques to measure time-dependent displacement fields in various geometric slices of the brain of human volunteers subjected to impulsive loading to the head. The heads of the volunteers were placed in one of two different fixtures that impart a mild impulsive load to the head.

The first fixture imposed an angular acceleration by rotating the head from one side to the other, ending with a hard stop. The second fixture imposes an impact to the forehead by moving the head forward until it contacts a comparatively rigid surface. After repeated impulsive loading, the Bayly team collected a sufficient amount of data from their experiments to create time-resolved displacement fields at a network of points in selected geometric slices of the brain. The displacements at these points were used to calculate the strains that occurred in each of the slices. These results, conducted on human tissue *in vivo*, provide excellent data with which to fine-tune and validate our constitutive models for the biological tissues comprising the brain. We did this by simulating the Bayly MRI tagging experiments with PRESTO using the finite element version of our head/neck model and comparing our results against those of the experiments.

##### 3.1.1 Head Rotation Experiment

Both the head rotation and head impact experiments, conducted by Bayly's group, employed mechanical fixtures that accelerated and abruptly stopped the head. This motion generated rotational and translational displacements in the brain that were measured by means of MRI tagging. Figures 4 and 5 display a schematic of the rotational fixture that imposed an impulsive angular acceleration to the head by creating a twisting motion about the longitudinal (spinal) axis (reprinted with permission from the author).

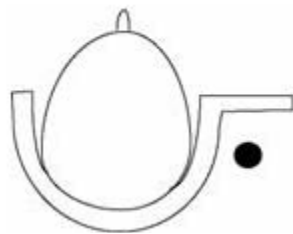


*Figure 4. Initial condition, prior to the twisting movement of the head. The black dot is the rotation stopper. (Reprinted with permission from the author).*

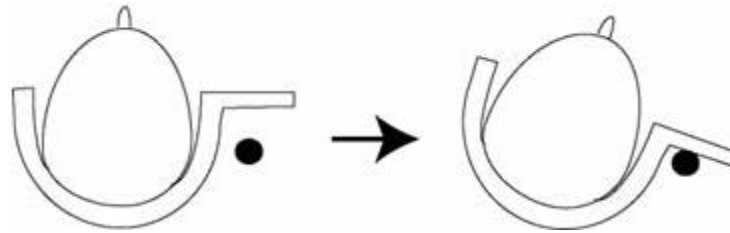


Figure 5. Initial-to-final configuration showing twisting movement of the head and the harness hitting the stopping mechanism. (Reprinted with permission from the author).

A weight, embedded in the fixture, was used to accelerate the head around the axis of rotation until it hit a built-in stop that abruptly ended the head motion. A typical angular rotation history experienced by the head during this experiment is shown in Figure 6.

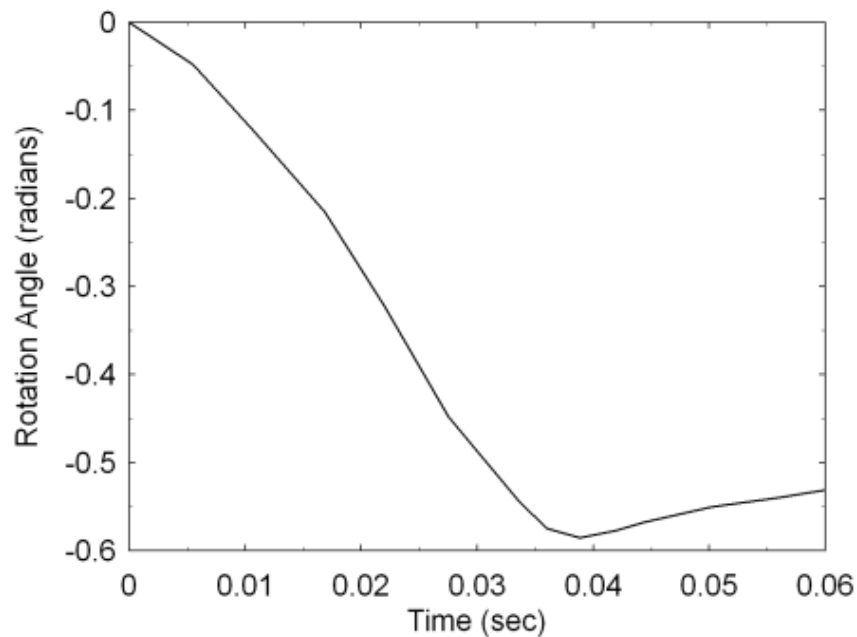


Figure 6. Typical angular rotation history imposed on the head in simulations of the Bayly experiments.

### 3.1.1.1 Finite Element Model

The finite element mesh for the head/neck model described in Section 2.1.1 was used to represent the head in our simulation of the Bayly rotational experiments. The model was simplified by excluding the sinus cavity air and the outer scalp/muscle elements. The sinus cavity air would have almost no influence on the behavior of the model in this type of problem. The scalp/muscle was left out because it resides outside of the skull and would not affect the behavior of the brain tissues within the cranium of the skull. Figure 7 shows the model used in our analysis.

The model was tilted slightly forward at the top of the head from what would normally be considered a vertical axis through the head. This was done to match the actual axis of rotation used in the experiments. The angular displacement history, defined in Figure 6 about the rotation axis, was imposed on the skull elements as a boundary condition to mimic experimental conditions. The materials within the cranium—the white and gray brain matter, falx and tentorium membranes, and the cerebral spinal fluid—were allowed to deform from the inertial effects caused by the rotation of the skull.

The constitutive models for the skull, falx, tentorium, and cerebral spinal fluid have been discussed in Section 2.1.2 and require no further explanation here. However, in order to capture the viscoelastic behavior of the white and gray brain matter in our PRESTO simulations, we were required to use a viscoelastic Swanson material model [25]. This model exhibits linear viscoelasticity coupled to an initial elastic response represented by the Swanson finite strain elastic model [26]. For this simulation, we have set the parameters of the viscoelastic Swanson model to emulate the generalized Maxwell model response described in Section 2.1.2 for the white and gray matter.

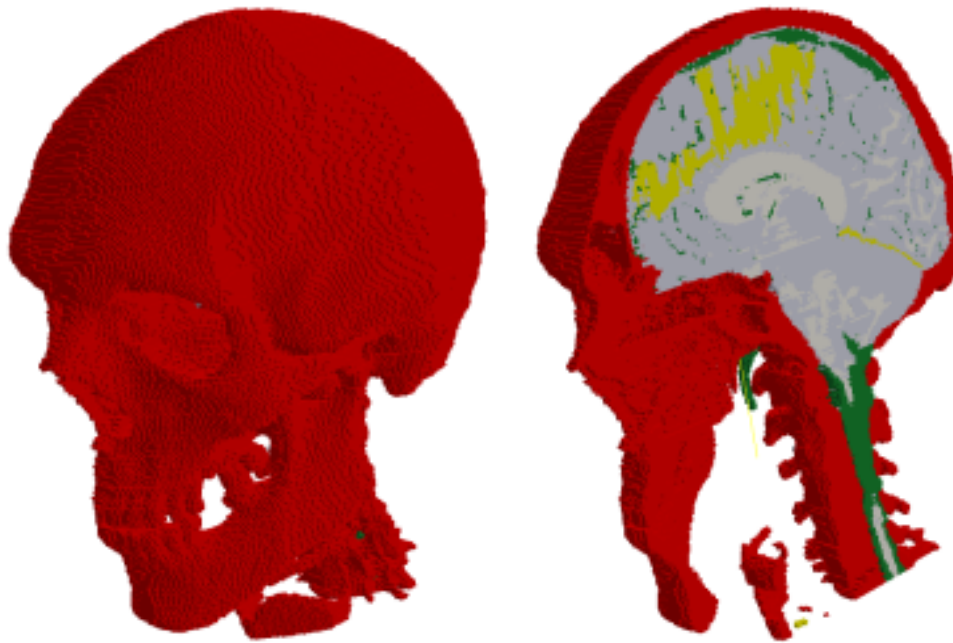


*Figure 7. Finite element head/neck model used in head rotation analysis. Sinus air and scalp/muscle has been removed from the model for this analysis.*

### **3.1.1.2 Comparison of Simulation to Experiment**

We initially conducted the Bayly rotation experiments using a viscoelastic decay constant  $\beta$  of 700/sec as reported by Zhang et al. [14] for the white and gray brain matter. This parameter determines how quickly material shear stresses relax in response to a shear deformation. Unfortunately, the  $\beta$  decay constant value of 700/sec dampened out our predicted shear strains far quicker than the experimental data displayed. As a result, we varied this parameter in our

simulations until we were able to match the experimental results and arrived at a decay constant of 40/sec. When simulating the rotation experiments using this latest value of  $\beta$ , our predicted shear strains persisted out to the longer times displayed by the experimental data. Consequently, we conducted the remainder of our validation simulations and all of our blast simulations with the modified value of 40/sec for  $\beta$  (see Table 2).

The shear strain data from the rotation experiments were collected within four spatial planes passing through various regions of the brain. Figure 8 shows the locations and the orientation of the planes used in their experiments. The reference plane, labeled “0 cm” in the figure, passes through both the genu (forward region) and splenium (posterior region) of the corpus callosum. The corpus callosum is a white matter structure that connects the left and right sides of the brain allowing for communication between the two sides. This structure transmits sensory, motor, and cognitive information between the brain hemispheres.

The Bayly paper presented shear strain data for points located within the plane labeled “+2 cm” (see Figure 8). This particular plane was located 2 cm in the superior direction from the “0 cm” reference plane and passes through the trunk (upper region) of the corpus callosum.



*Figure 8. Location of the planes used in the experiments. (Reprinted with permission from the author).*

Figure 9 displays our predictions of the shear strain histories from the PRESTO simulations for points in the +2 cm spatial plane. The results are shown for only those times after the head-rotating fixture has hit the built-in stop. The stopping of the head rotation provided the largest shear strains in the brain tissue.

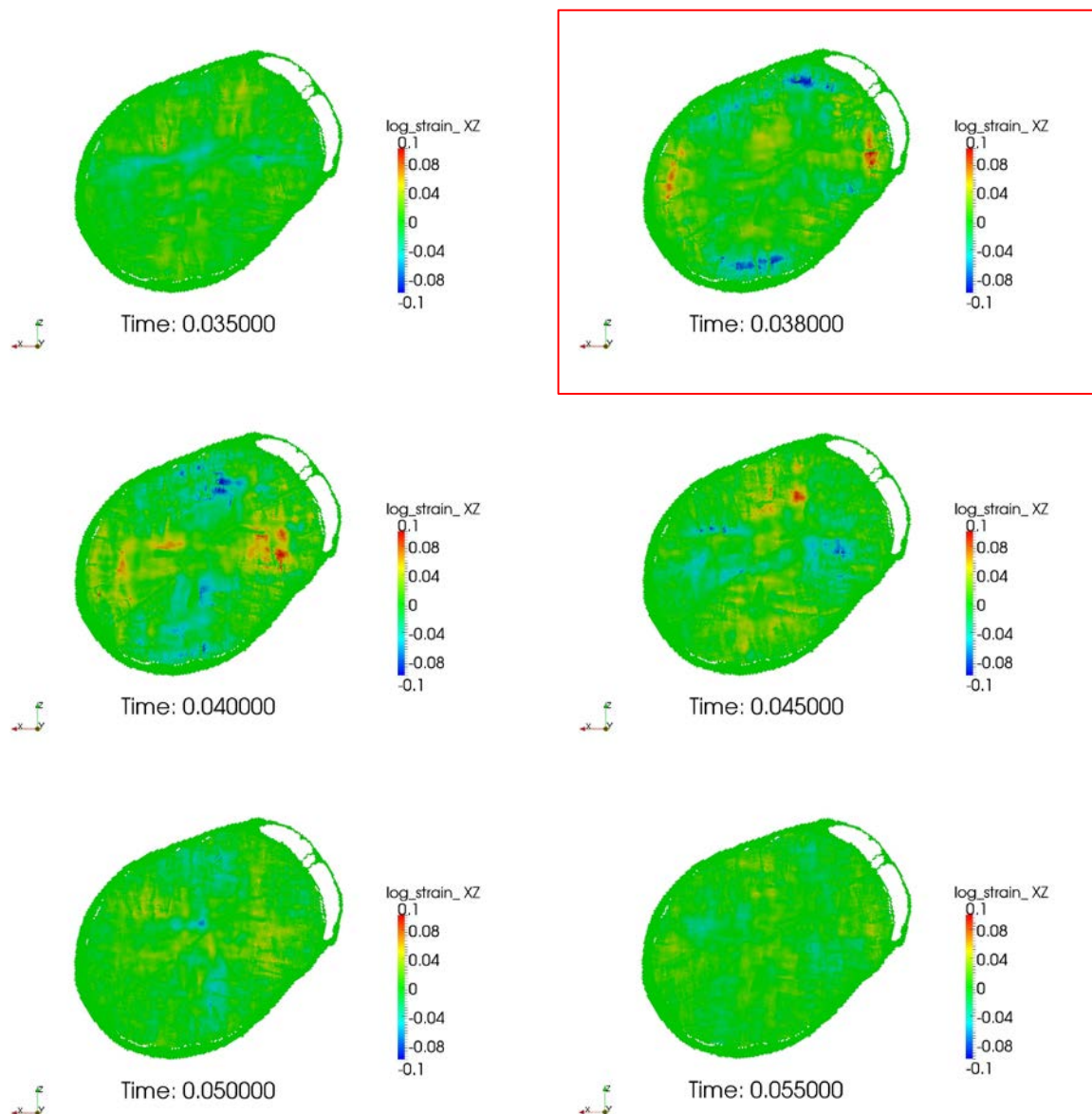


*Figure 9. Calculated shear strains from PRESTO simulation at selected times on the “+2 cm” plane. The 38 ms time, indicated in a red box, was used as a specific comparison to the Bayly experimental results.*

Selected images displaying shear strain magnitudes at various times during the rotation experiment are shown in Figure 10 for subjects 1 and 2. These were calculated by the Bayly research team from the displacements measured at the network of points in the “2 cm” plane by means of the MRI tagging procedure. The difference in timing fiducials between our simulation and the experiments is such that our predicted shear strain plot at 38 msec (Figure 9) corresponds to the 228 msec plot (Figure 10) of the experiment.

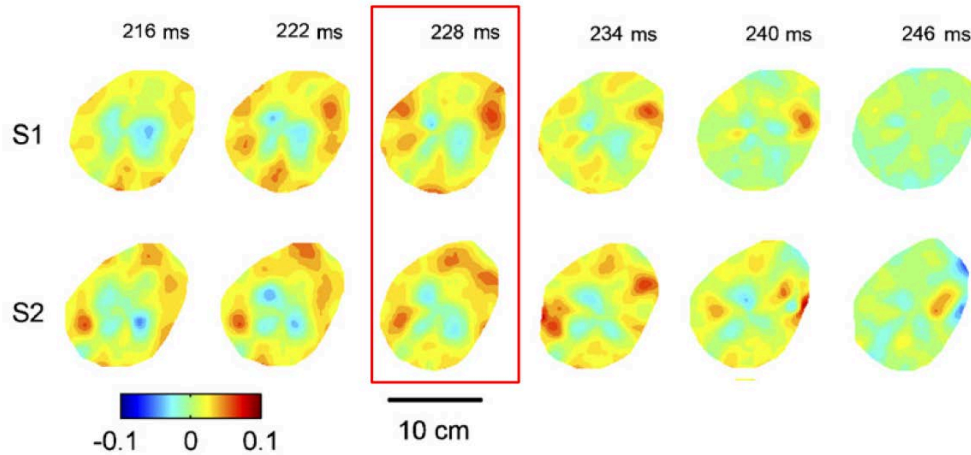


Figure 10. Calculated shear strains at selected times from Bayly's head rotation experiment. (Reprinted with permission from the author). The 228 ms time, indicated in a red box, was used as a specific comparison to the PRESTO simulation results.

The predicted values of maximum shear strain and the locations of these maxima from our finite element analysis matched the experimental data moderately well. By changing the viscoelastic decay constant for both the white and gray matter, we were able to match the duration of the strain maxima observed in the experiments. However, we did not match the areal extent of the strain maxima. In fact, our simulations predicted maximum strain regions of significantly smaller area (see Figure 9) relative to what was displayed in the experiment results (Figure 10). Some of this discrepancy is the result of the differences in the spatial refinement of the data. Our analysis used one *millimeter* spacing between finite element nodes while the experiment used spacing on the order of one *centimeter*. The larger mesh spacing would force one to draw contour plots (as seen in Figure 10) with only a few dozen mesh points to define a strain field from the measured displacements as opposed to being able to use thousands of points to define these fields from our finite element analysis. Other sources of error, which could account for the differences in the predicted and observed areas of maximum shear strain, remain a topic for further work.

### 3.1.2 Forehead Impact Test

#### 3.1.2.1 Experimental Conditions

The second MRI tagging experiment, performed by Feng et al. [18], subjected three healthy individuals to mild head impact using a fixture that accelerated the forehead of the test subject onto a fixed pad within the confines of an MRI machine. Figure 11 shows a schematic of the resultant head motion. In this experiment, the head experiences translation parallel to the mid-sagittal plane of the subject's head and rotation about an axis normal to this plane.

Skull displacement histories in the anterior-posterior (horizontal) and superior-inferior (vertical) directions and angular displacement of the skull about a rotation axis normal to the sagittal plane are shown in Figure 12 for a typical impact. The conditions of the experiment were such that the subjects' heads were constrained to planar motion parallel to the mid-sagittal plane. (plane of Figure 11a).

The displacement data in Figure 12 was measured for experimental Subject S1 and represents the typical rigid-body motion of the skull during the experiments. We have used this data to define the kinematic boundary conditions imposed on our head/neck model in order to simulate this series of experiments.

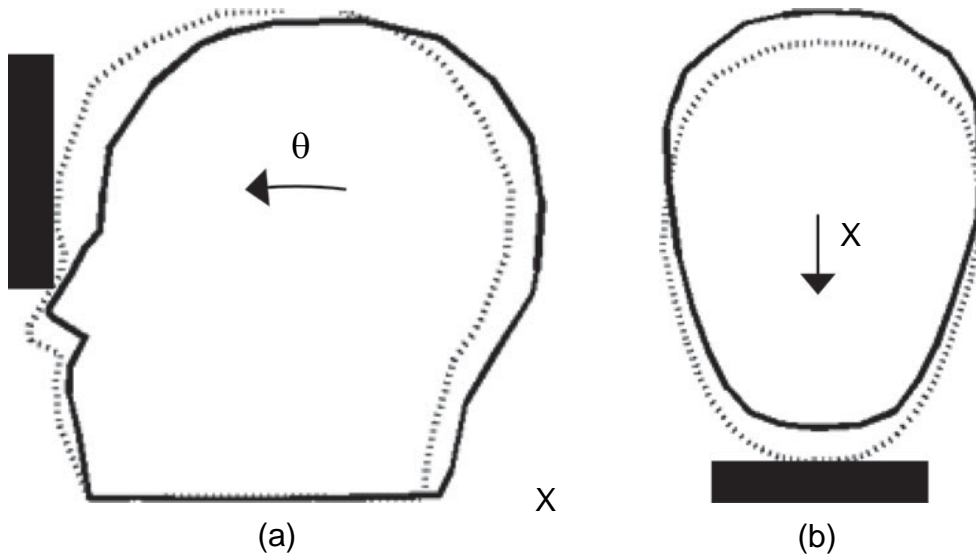


Figure 11. Direction of head travel. Image (a) displays the mid-sagittal plane. (Reprinted with permission from the author).

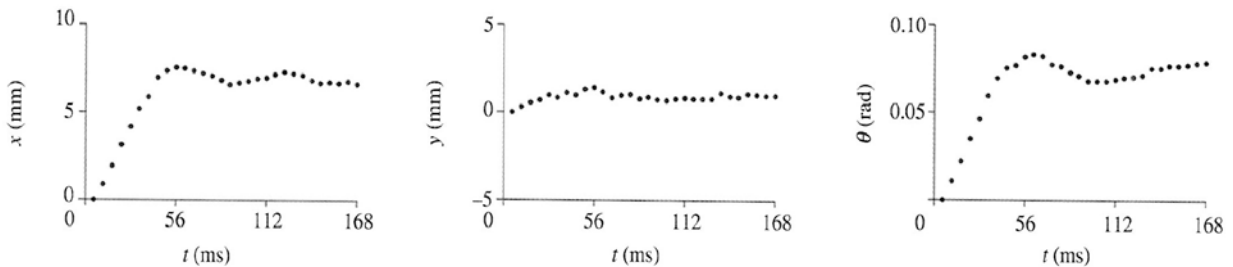


Figure 12. Rigid-body motion of the skull versus time. (Reprinted with permission from the author).

Specifically, Figure 12 shows that during the experiment, the rigid-body motion of the subject's head translates approximately 7 mm in the X-direction and rotates 0.07 radians (4 degrees) before it impacts the stopper pad. The maximum linear and angular accelerations associated with this motion occurred at 44.8 msec and 39.2 msec, respectively. The middle plot in the figure shows that the head translates very little in the superior- inferior (vertical) direction.

In order to simulate these experiments, we employed the finite element head/neck model used for the rotational experiments presented in Section 3.1.1. The details of this model have already been discussed in Section 3.1.1.1. To simulate the experimental impact event, we applied a rigid-body motion to the skull of our model by imposing the linear and angular displacement histories

displayed in Figure 12. We applied rotation about an axis normal to the mid-sagittal plane passing through the neck 10.2 cm below the foramen magnum of the skull.

### 3.1.2.2 Comparison of Simulation to Experiment

The impact experiments of Feng et al. [18] calculated spatial displacement and maximum principal strains at four sites in the brain relative to the skull for the duration of each experiment. These sites were located in a sagittal plane positioned in the left hemisphere parallel to, and offset 1 cm from, the mid-sagittal plane of the brain. The four sites, labeled **a** through **d**, are shown in Figure 13. Site **a** is located in the frontal lobe, site **b** in the parietal region, site **c** is in the cerebellum, and site **d** is near the pituitary stalk.

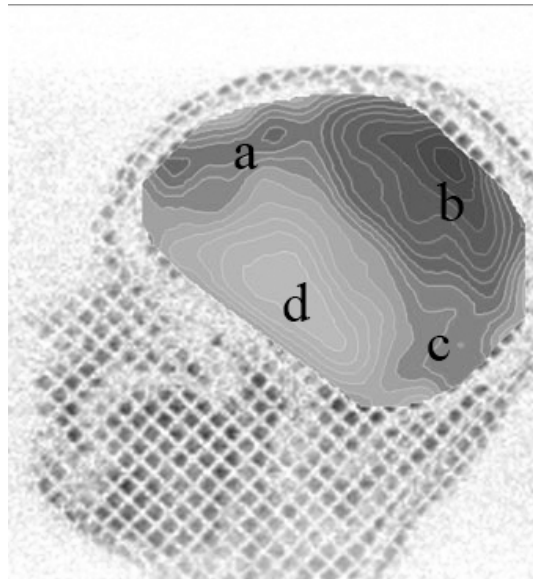


*Figure 13. The four sites in the brain where displacement and strain were calculated in the impact experiments. (Reprinted with permission from the author).*

Experimentally derived plots displaying relative displacement at locations **a-d** with respect to a reference point located at the foramen magnum of the skull are shown in Figure 14 for three different test subjects.

Our prediction of relative displacement at these locations is shown in Figure 15. As shown in the figure, all of our predicted displacements display a maximum value of approximately 0.9 mm 55 msec after the onset of head motion. This compares well with the experimental data displayed in Figure 14 for all three test subjects. However, our simulations under-predict the maximum displacements at locations **a** and **b** for all three subjects and slightly over-predict the displacements at locations points **c** and **d**. Our simulations best matched the displacement data of Subject S2, especially at locations **a** and **c**. In essence, our predictions of relative displacements appear to fall within the range of those displayed by the test data.

Further evidence of variation in the experimental data among the three test subjects is displayed in Figure 16 by comparing the time-lapse sequences of relative displacement magnitudes. The

figure shows how much the displacements differ between test subjects as well as the degree of spatial variation of the displacements within the brain. For example, Subject S2 experienced roughly half the maximum displacement (at location **b**) relative to that experienced by Subject S1.

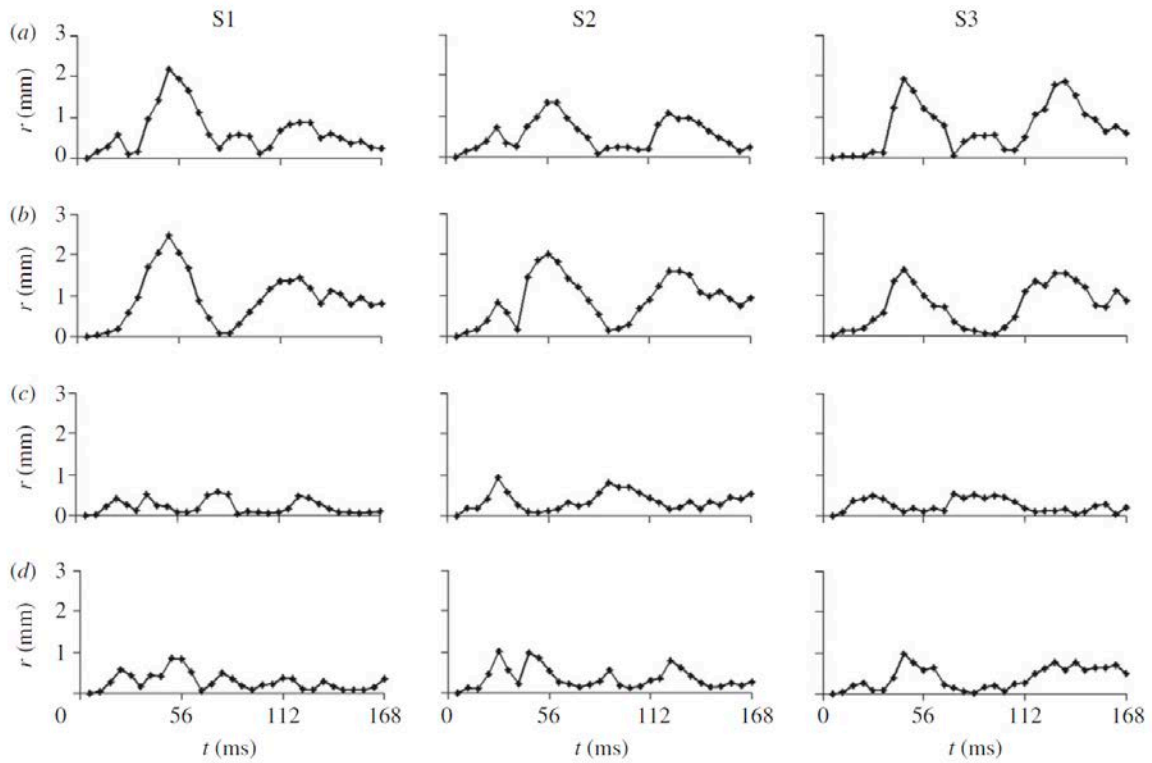


Figure 14. Measured displacement at four locations for three different test subjects. (Reprinted with permission from the author).

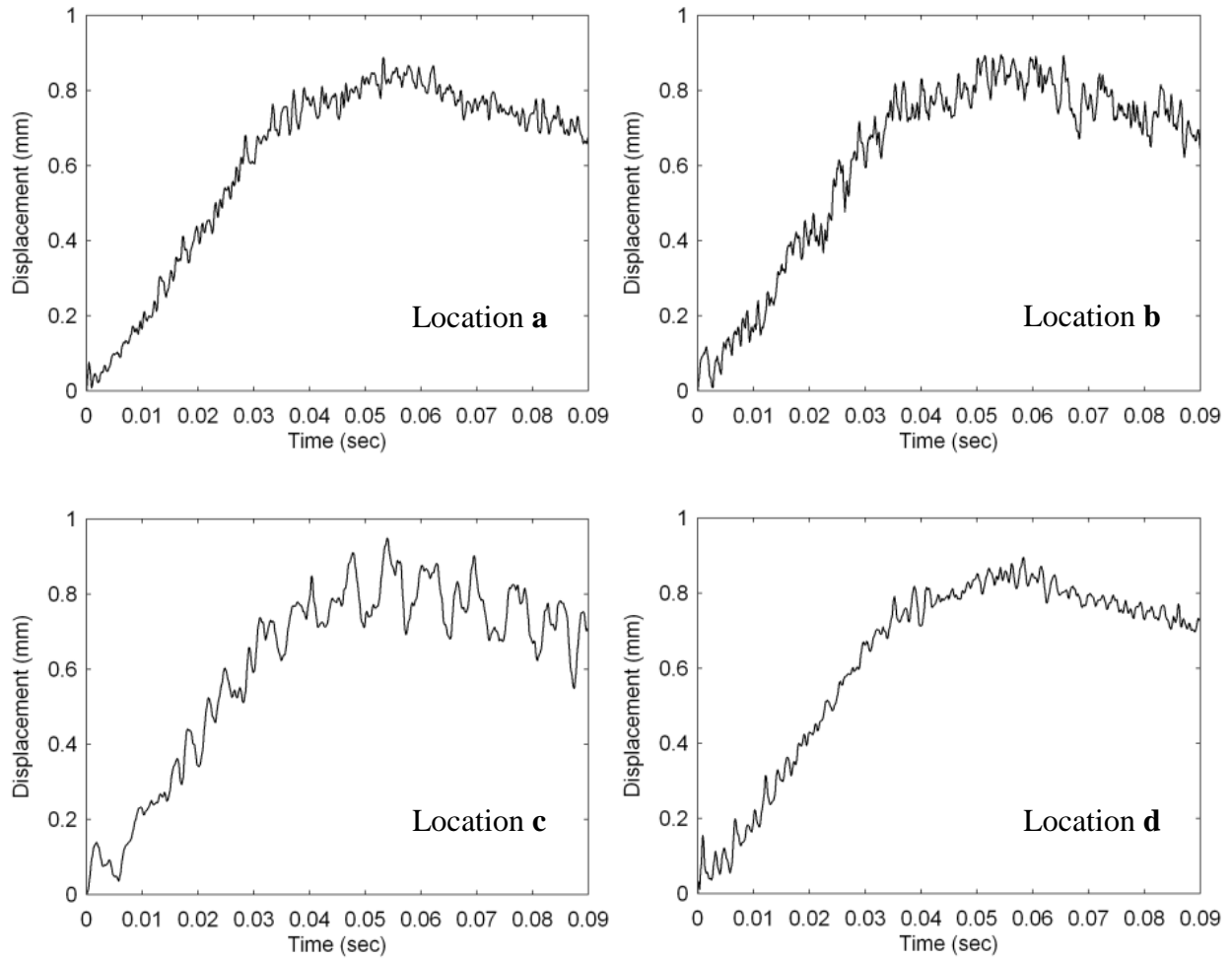
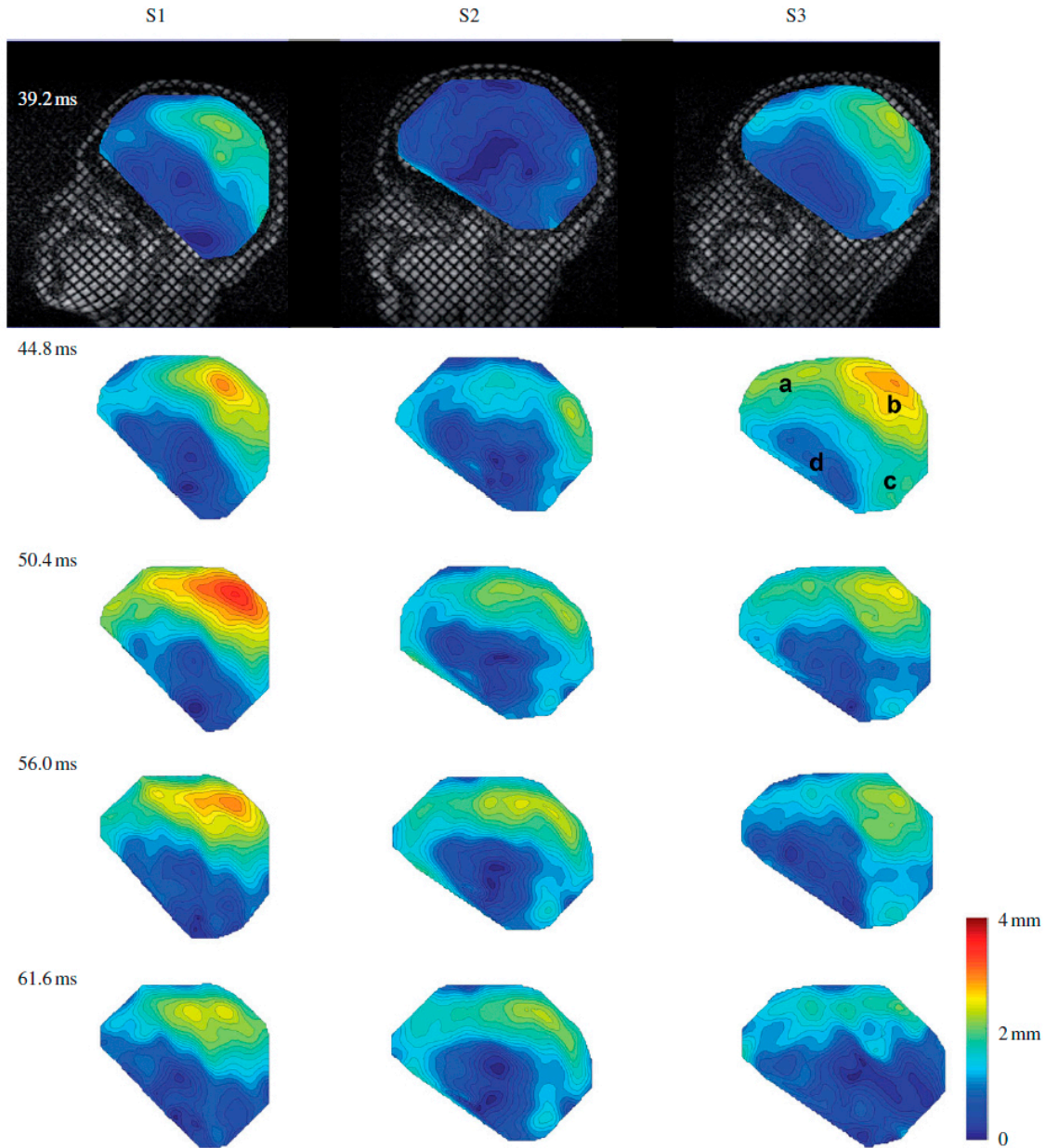


Figure 15. Simulation predictions of relative displacement at four locations (a-d) in the brain.



*Figure 16. Calculated displacements relative to the skull for three test subjects. (Reprinted with permission from the author).*

In view of the variation in displacement history exhibited by the experimental data and the fact that our simulations predict displacement histories bracketed by this experimental variation, we submit that our simulation toolset possesses the capability to model intracranial stress wave mechanics during impulsively loading events to the head. This conclusion is reinforced with the comparison to data we provide in the next section.

### 3.2 Simulation of APL Field Blast Data

To exercise our modeling and simulation toolset, we conducted simulations of direct blast exposure of our head/neck model from three principal directions, front, rear, and lateral (right side), (see Figure 17).

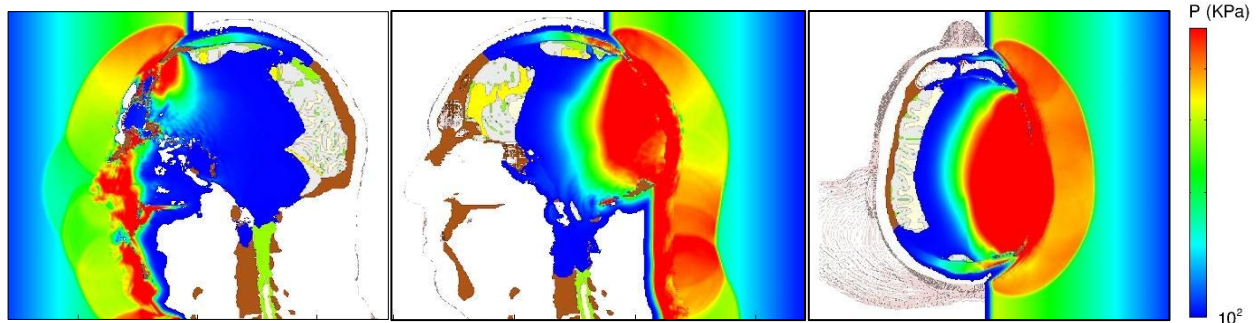


Figure 17. Stop-action plots of blast-induced pressure waves propagating through the head from the front (left), rear (center), and lateral (right) directions.

Originally, we selected blast conditions within the marginal limits of blast pressure and pulse width for threshold lung damage, as defined by the corrected Bowen survivability curve for primary blast injury [27]. These conditions were chosen for two reasons. First, they are similar to those predicted to occur at a location 2-to-3 meters distant from a detonated explosive device constructed from a 3 kg charge of Octol explosive. Second, these conditions represent a limiting case for blast exposure that is predicted to be survivable by the Bowen lung damage criterion. These simulations generated a 1.3 MPa (13 bars) pressure pulse similar to that shown in Figure 18. However, for this blast condition, our results predicted that the 13 bar blast generated intracranial stress and energy levels that were too great to be associated with mild to moderate traumatic brain injury and, in addition, caused a fair amount of facial bone fracture [28].

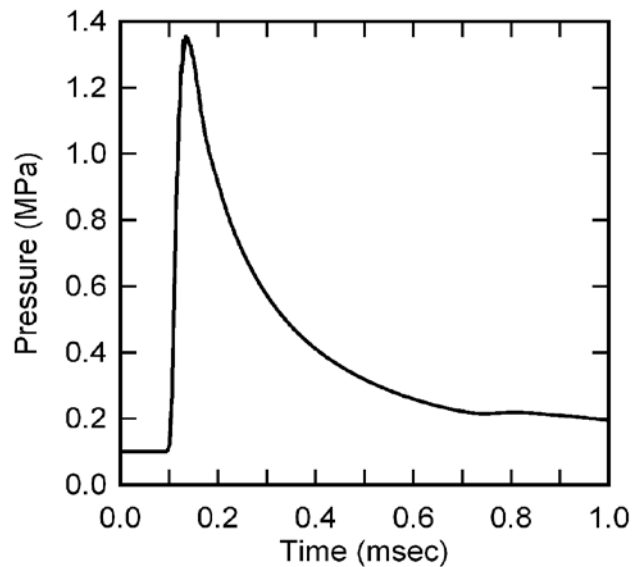


Figure 18. Pressure pulse generated by a 1.3 MPa (13 bars) of blast wave.

As an alternative, we selected blast conditions similar to those defined in the APL field test series [21]. There, APL researchers subjected their Human Surrogate Head Model (HSHM) to free field frontal blast conditions resulting from a 5 lb. charge of Composition-4 (C-4) suspended 92 inches from the head model (see Figure 19). These conditions resulted in an air blast of magnitude 3.6 bars (0.36 MPa) when it encounters their Human Surrogate Head Model. A profile of this blast pulse is displayed in Figure 20.

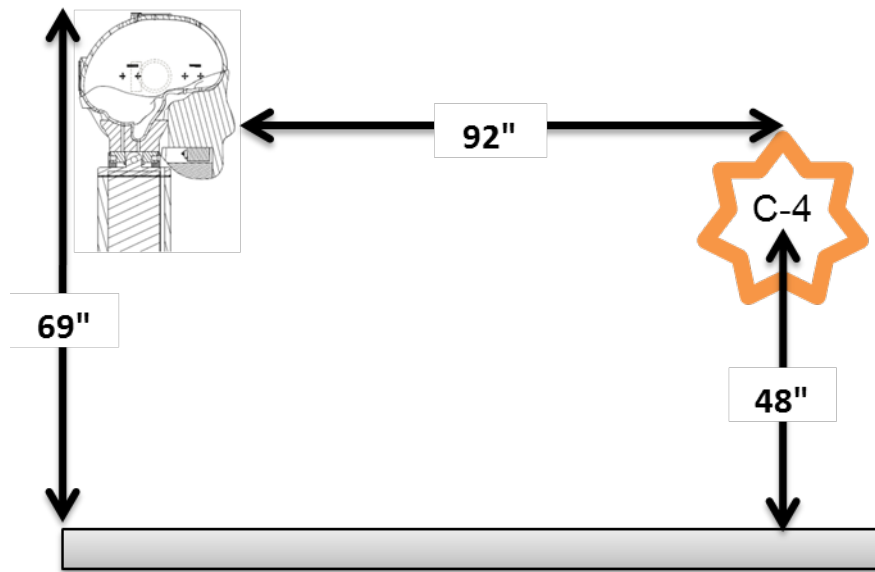


Figure 19. Test configuration of the APL field test blast experiments on their Human Surrogate Head Model (HSHM).

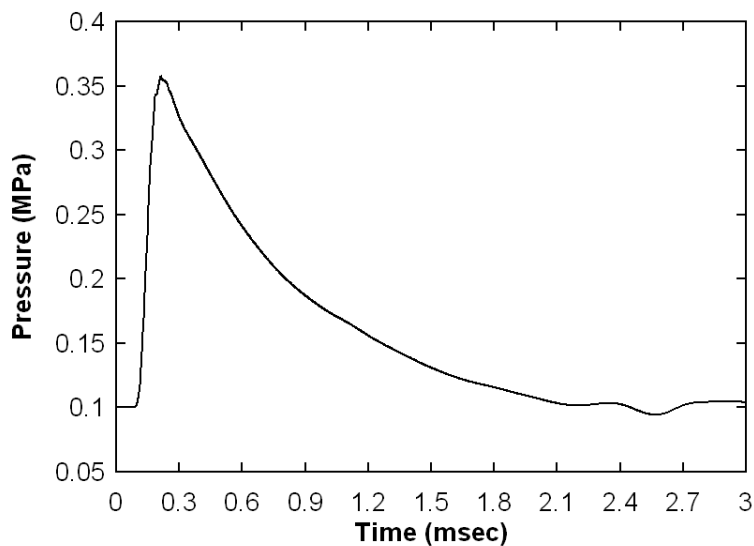
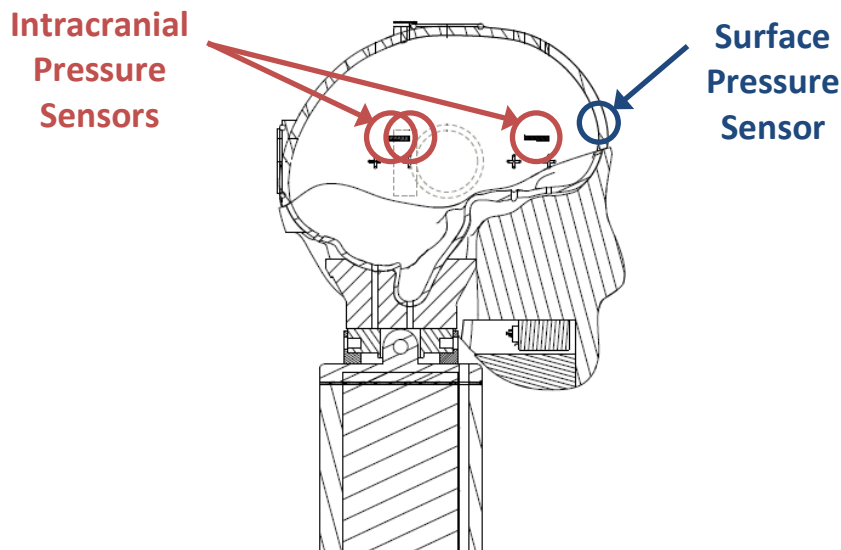


Figure 20. Pressure pulse of 0.36 MPa (360 KPa) magnitude generated in APL blast experiments on their Human Surrogate Head Model (HSHM).

Our simulation of the APL field tests were performed by positioning our head/neck model within an environment of air at ambient conditions. To create the blast wave, we positioned a slab of energized air, held at conditions of elevated energy and pressure, and positioned approximately 16 cm from the head at time zero. At times greater than zero, air mass flow is permitted to occur from the energized slab, creating a pressure pulse that propagates in the direction of the head/neck model. The amplitude and pulse width of the blast wave is determined by setting the energized air to predefined conditions of energy, pressure and slab thickness. By the time the pressure pulse reaches the head, its amplitude has degraded to 0.36 MPa, possessing a profile identical to that appearing in Figure 20.

From our simulation results, we collected spatial distributions of stress and energy maxima experienced throughout the brain over the full course of the blast event. However, the APL experiments only monitored pressure histories of sensors placed at four locations in their head model. One sensor was located on the forehead, one in the anterior (frontal) brain region and two in the posterior region close to the mid-sagittal plane of the HSHM brain. A diagram of sensor location is shown in Figure 21.



*Figure 21. Diagram of sensor placement in the APL Human Surrogate Head Model (HSHM).*

A typically blast simulation with the head/neck model required 31 cpu-hours per millisecond of simulated time using 96 processors on the Sandia National Laboratories Red Sky computer system. A simulation that also includes the helmet model required roughly 20% additional time to execute.

### **3.2.1 Simulation Results**

Figures 22 and 23 display a series of time-lapse images of pressure as the blast wave interacts with our head/neck model generating dilatational (pressure) waves that propagate through the scalp, skull, and into the brain. This wave action is rather quick with the dilatational waves propagating through the brain and dissipating within the first 2 milliseconds of exposure. Since the biological materials comprising the head also support shear, the blast wave also generates shear waves that propagate through the head at a speed slower than that of the dilatation waves. A set of time-lapse images of the effective (shear) stress are plotted in Figures 24 and 25.

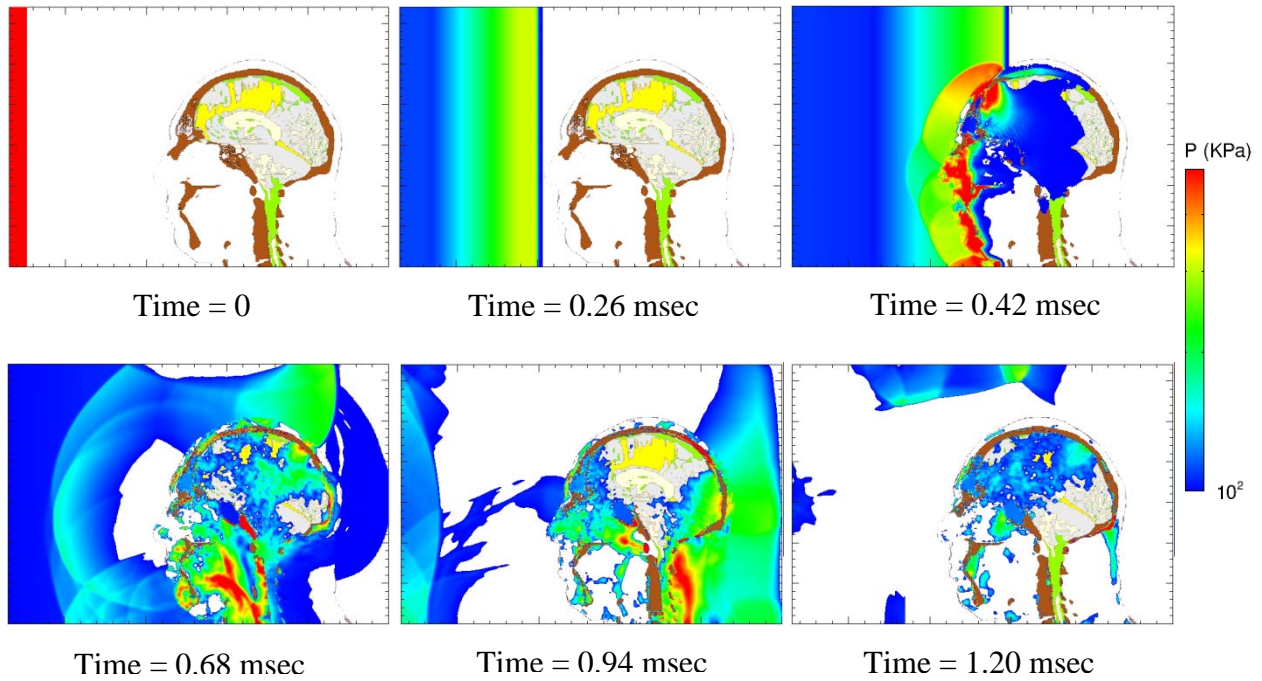


Figure 22. Time-lapse images of frontal blast exposure showing pressure in the mid-sagittal plane of the head/neck model. Upper pressure limit is 500 KPa. Regions without color are at or below the threshold pressure of 1 atmosphere (100 KPa).

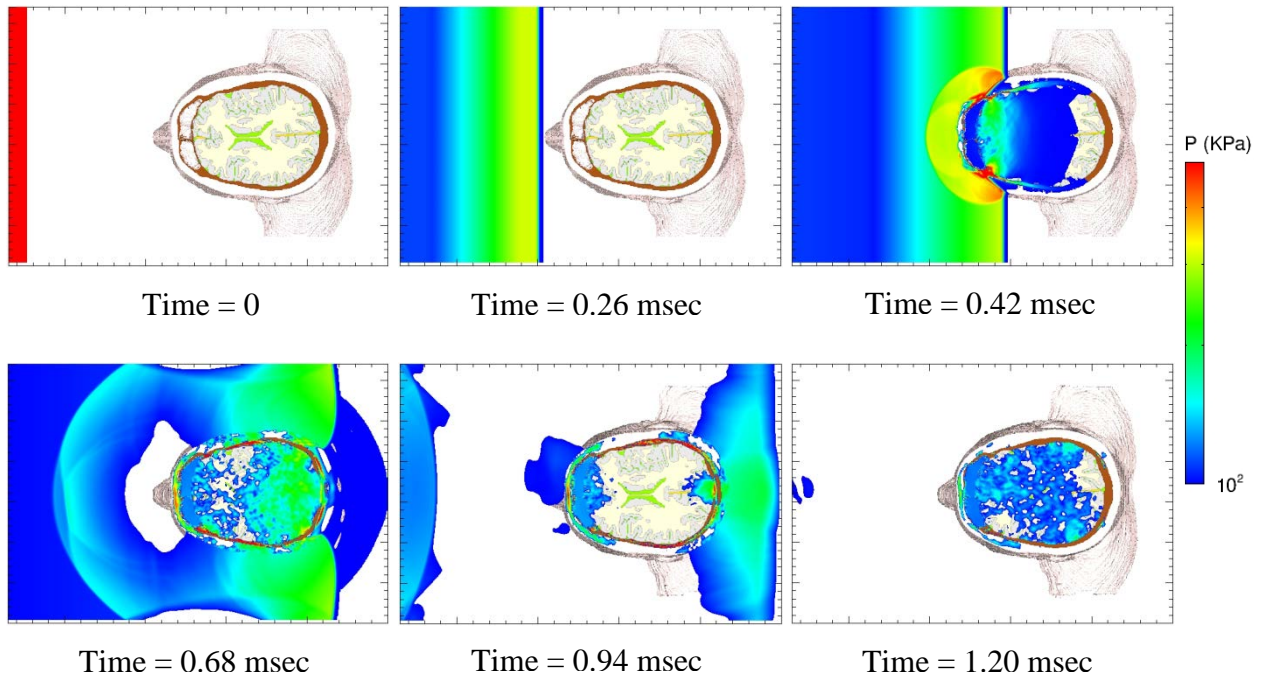


Figure 23. Time-lapse images of frontal blast exposure showing pressure in an axial plane just about the orbits of the head/neck model. Upper pressure limit is 500 KPa. Regions without color are at or below the threshold pressure of 1 atmosphere (100 KPa).

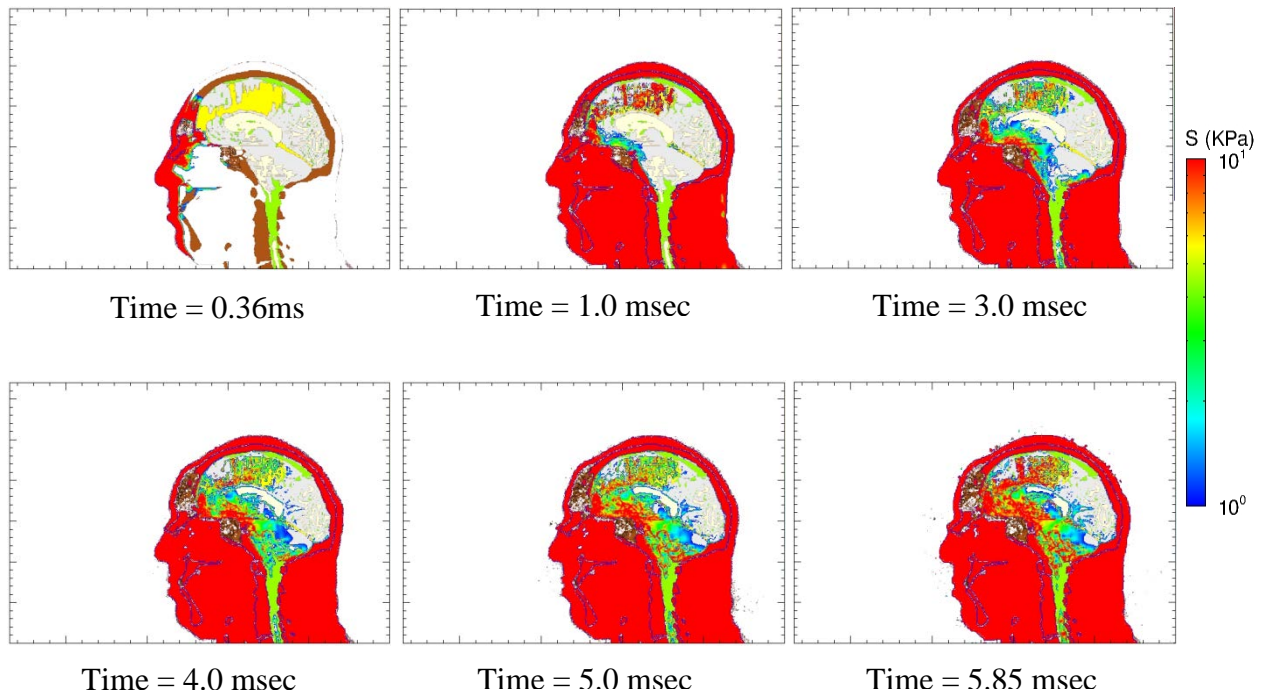


Figure 24. Time-lapse images of frontal blast exposure showing effective (shear) stress levels in the mid-sagittal plane of the head/neck model.

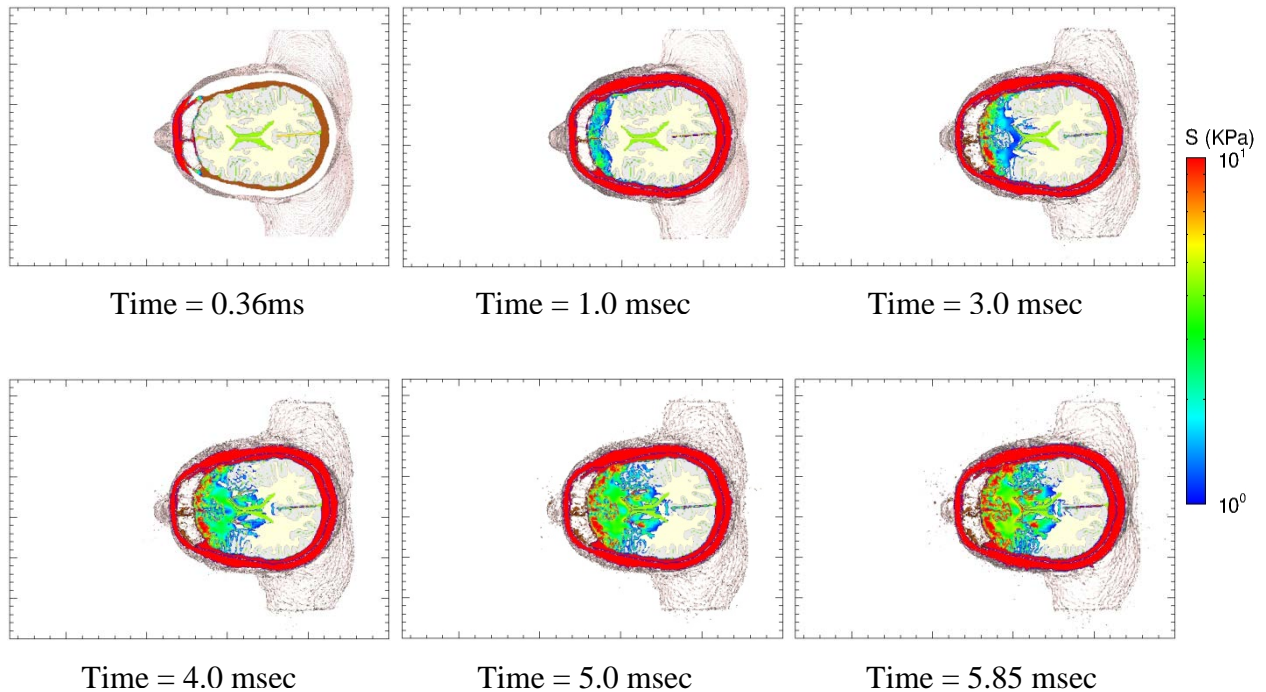


Figure 25. Time-lapse images of frontal blast exposure showing effective (shear) stress levels in an axial plane just about the orbits (eye sockets) of the head/neck model.

We also placed Lagrangian tracer points within our head/neck model that correspond to the forehead and intracranial sensor locations of the APL blast tests conducted on their HSHM. Our frontal blast simulation was set up to mimic the APL test as closely as possible so that we may compare our predictions of intracranial pressure to those measured in the APL tests. A comparison of our simulation predictions with those of the APL test are shown in Figure 26.

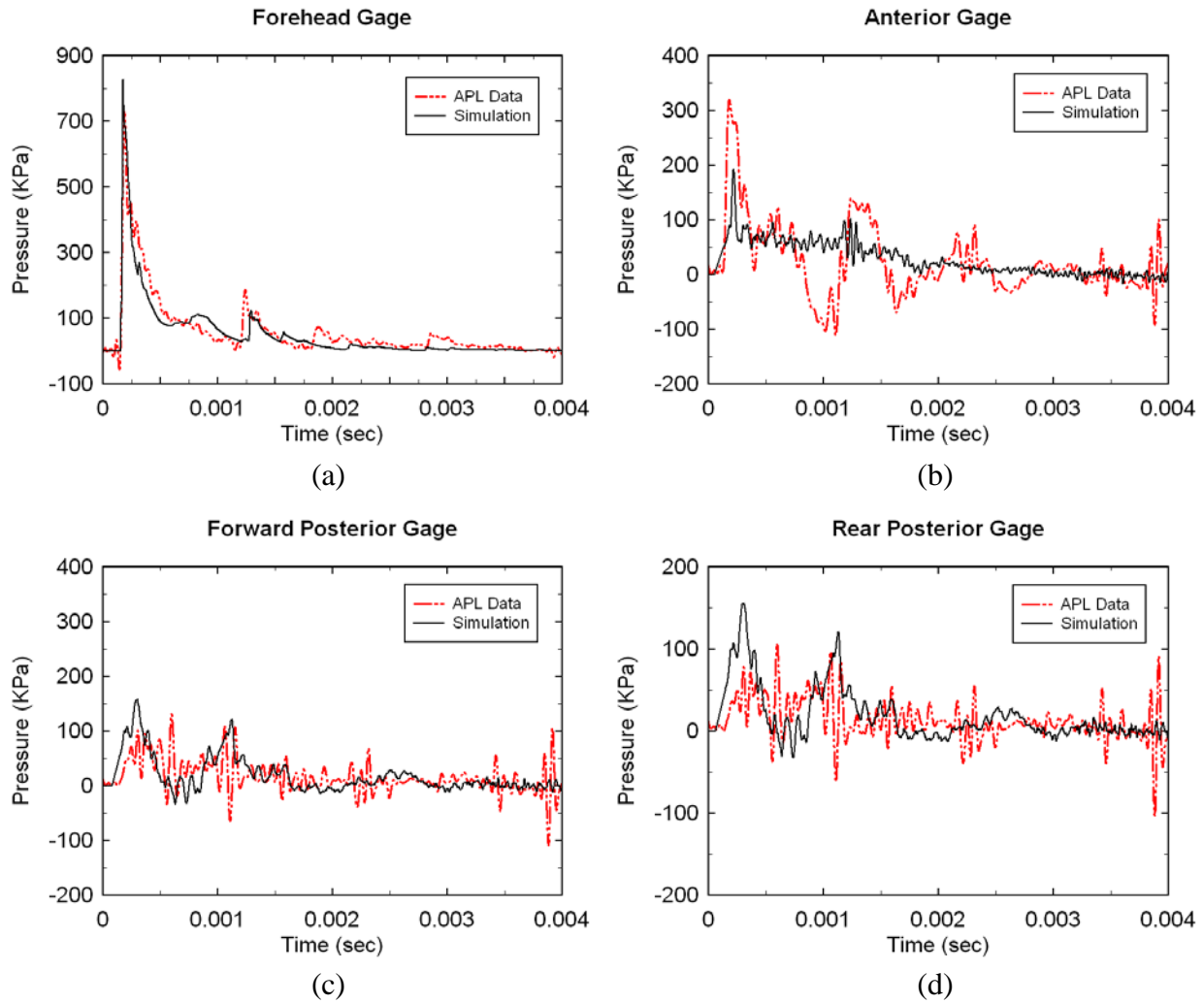


Figure 26. Comparison of simulation predictions with the APL blast test pressure data taken from their Human Surrogate Head Model (HSHM) for a 3.6 bar (360 KPa) frontal blast.

The pressure plots displayed in Figure 26 suggest that the simulation predictions compare reasonably well with the pressures measurements recorded in the APL blast experiment. The forehead pressure histories displayed in Figure 26a show the best agreement and reflect the accuracy of our equation-of-state representation for air. The most significant difference appears in Figure 26b between the experimental and predicted pressure histories for the anterior intracranial gage. This difference is likely due to the fact that the Sandia head/neck model possesses a frontal sinus cavity that attenuates the pressure pulse before reaching the anterior gage location whereas the APL human surrogate head model does not include any such cavity.

This distinction suggests that a more realistic representation of biological structure is necessary to capture naturally occurring wave attenuation within the cranium.

The better agreement between our simulation predictions and the APL pressure data at the posterior gage locations (see Figures 26c and 26d) is somewhat surprising considering the influence of the frontal sinus cavity, as described above. This agreement may be coincidental.

In view of mixed agreement between simulation and experiment as identified in Figure 26, more comparisons between the two approaches should be undertaken to resolve this issue. Even if both of these approaches agree, it is still not clear which is more accurate at representing living biological materials under impulsive loading. It is our view that digital simulation has the ability to be more accurate since it permits a higher fidelity representation of biological structure and material response than can be provided by physical models composed of synthetic materials devoid of fine-scale structures such as membranes, blood vessels, and sinus cavities.

## 4 BLAST SIMULATIONS OF UNPROTECTED HEAD

In this section, we present simulation results of blast loading of the unprotected head/neck model when it is exposed to the 3.6 bar (360 KPa) blast wave from the front, side, and rear directions. Specifically, we would like to answer the following question: are the locations of elevated stress wave energy levels in the brain dependent on the direction from which the blast originates or do they tend to occur in the same locations regardless of blast direction?

### 4.1 Stress Wave Magnitude versus Energy

Before we present simulation results on blast direction dependence, we present the following argument in support of monitoring wave energy, rather than stress magnitude, as the more useful wave physics variable to correlate with brain injury and helmet protection.

Figure 27 displays the maximum compressive and tensile pressure, deviatoric stress, and the energies associated with those stresses in the mid-sagittal plane for the 360 KPa frontal blast. These are plots of the maximum values of stress and energy that have occurred over the complete duration of the simulation lasting just over 5 msec. Plots (a), (c), and (e) of Figure 27 reveal focal regions in the brain experiencing significant levels pressure and deviatoric stress in the first 5 msec of blast exposure. Specifically, maximum levels of 1.0 MPa compressive pressure, 0.2 MPa of tensile pressure, and 20 KPa of deviatoric (shear) stress are predicted to occur within the brain before the onset of any significant head accelerations. In fact, the intracranial stress wave formation, propagation, and focusing events are predicted to occur before the head moves 2-4mm in response to the blast.

The associated energy distributions are displayed in images (b), (d), and (f) of Figure 27. Specifically, Figure 27b displays the maximum isotropic compressive energy distribution over the full simulated time, Figure 27d shows the maximum isotropic tensile energy, and Figure 27f shows the maximum deviatoric (shear) energy distribution. Isotropic compressive energy is the energy associated with volumetric crush. Isotropic tensile energy is associated with dilatation, a stress condition that could give rise to cavitation which has been hypothesized to cause brain damage [29,30].

And finally, deviatoric strain energy is associated with shearing that could lead to tissue tearing. For the 360 KPa frontal blast scenario shown in Figure 27, the brain experiences focal regions of  $300 \text{ J/m}^3$  isotropic compressive energy,  $200 \text{ J/m}^3$  isotropic tensile energy, and  $300 \text{ J/m}^3$  shear energy. Furthermore, our simulations predict greater spatial variation in the maximum energy distributions throughout the brain than are displayed by their stress counterparts.

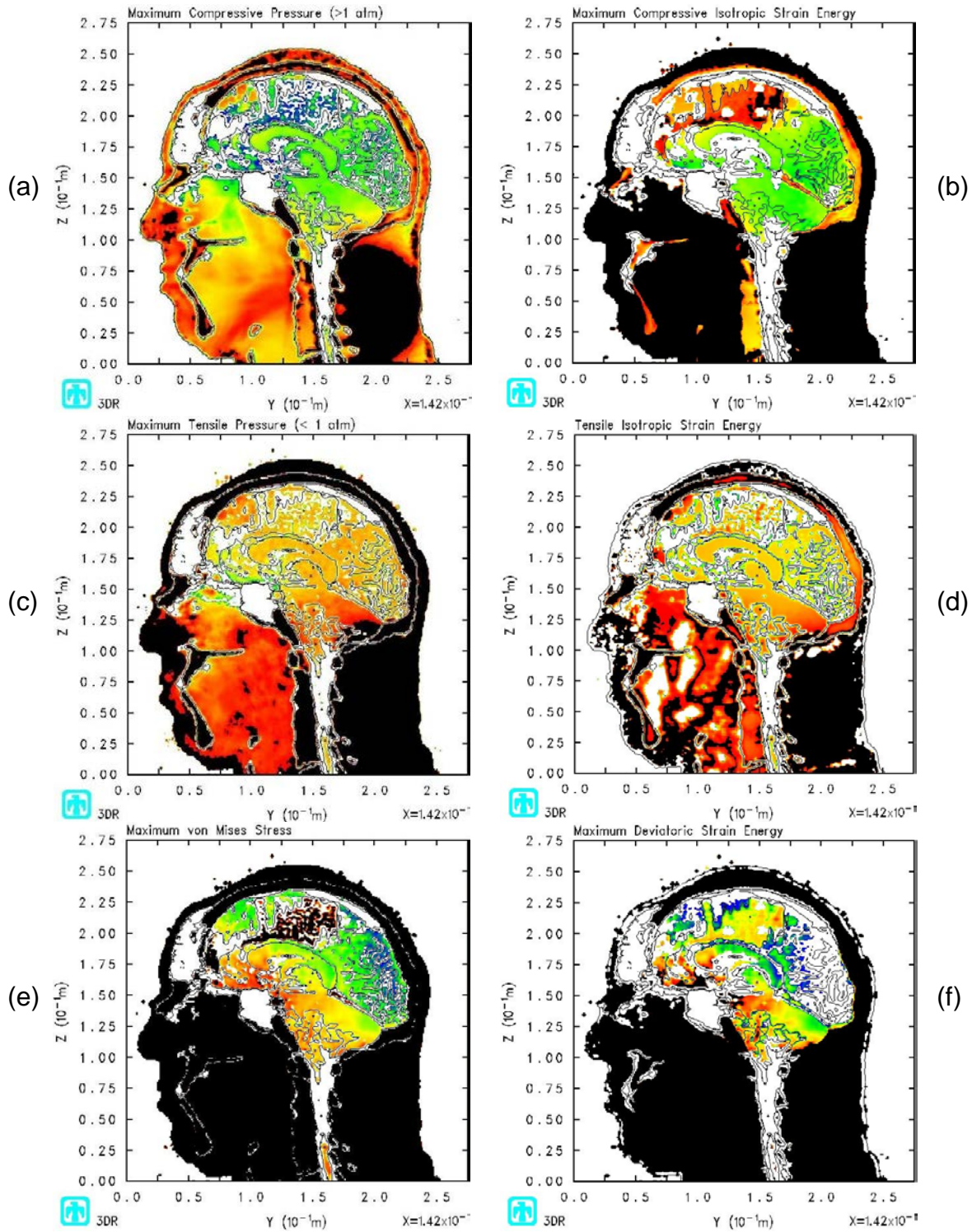


Figure 27. Plots of maximum stress and energy in the mid-sagittal plane for a 360 KPa frontal blast. (a) Maximum compressive pressure (blue: 0.1 MPa; red: 1 MPa) and (b) corresponding isotropic compressive energy (blue: 1 J/m<sup>3</sup>; red: 300 J/m<sup>3</sup>). (c) Maximum tensile pressure (blue: 1 KPa; red: 200 KPa) and (d) corresponding isotropic tensile energy (blue: 1 J/m<sup>3</sup>; red: 200 J/m<sup>3</sup>). (e) Maximum deviatoric (shear) stress (blue: 0.1 KPa; red: 20 KPa) and (f) corresponding

shear strain energy (blue:  $1 \text{ J/m}^3$ ; red:  $300 \text{ J/m}^3$ ). Plot variable levels increase from blue (minimum), green, yellow, and red (maximum). Black denotes that the plot variable max limit has been exceeded.

This result is illustrated in the plots of maximum stress and associated energy distributions appearing in Figure 27. This is particularly true for the isotropic compressive energy when compared to pressure but less so for the isotropic tensile and deviatoric (shear) energies versus their respective stress counterparts. These energy quantities take into account not only the stress level, but also the corresponding deformation associated with that particular stress. We determine these energy variables using the following relations.

$$\text{Isotropic Energy} = \int P \frac{d\rho}{\rho}, \quad \text{Deviatoric (Shear) Energy} = \int \text{tr}(\mathbf{S}\mathbf{d})dt, \quad (4)$$

where  $P$  denotes pressure (positive in compression),  $\rho$  is mass density, and  $\mathbf{S}$  and  $\mathbf{d}$  are the deviatoric stress and rate of deformation tensors, respectively. The deviatoric stress power term  $\text{tr}(\mathbf{S}\mathbf{d})$  denotes the trace of the tensor multiplication of  $\mathbf{S}$  and  $\mathbf{d}$ . In index notation, this term is defined as

$$\text{tr}(\mathbf{S}\mathbf{d}) = S_{ij}d_{ij}. \quad (5)$$

*Isotropic Compressive energy* is calculated from eq.(4)<sub>1</sub> whenever  $P$  is positive (compressive) whereas the *isotropic tensile energy* is determined from eq.(4)<sub>1</sub> whenever  $P$  is negative (tensile).

Although our simulation may predict a high stress level within the brain, the associated energy level will only be high if the stress has also induced a significant deformation. Consequently, both stress and its associated deformation must be substantial to predict a significant energy level. We suspect that high stress levels alone are not adequate metrics of tissue damage and that stress must also be accompanied by a significant deformation in order to create favorable conditions that induce tissue damage. Consequently, we will use isotropic and shear energies as our principal metrics rather than stress magnitudes when discussing conditions leading to localized brain damage.

## 4.2 Influence of Blast Direction

Figure 28 presents a comparison of maximum isotropic compressive energy distributions in the mid-sagittal and axial planes of the head/neck model as a function of blast direction, specifically frontal, right side, and rear blast directions.

Figure 29 compares the maximum isotropic tensile energy distributions from the frontal, side, and rear blast simulations for the same anatomical planes in the head/neck model.

Finally, Figure 30 displays the maximum deviatoric (shear) energy distributions for the three blast directions.

Note that the isotropic compressive energy distributions in the brain vary as a function of blast direction where the greater deposition of energy occurs in the region of the brain closest to the blast source. Thus, isotropic compressive energy deposition is greatest in the frontal brain lobes for the front blast, in the occipital region for rear blast, and right temporal lobe for right side

blast. However, the same dependence on blast direction does not appear to be the case for the isotropic tensile energy and deviatoric energy, as seen in Figures 29 and 30, respectively.

The fact that the simulations do not uniformly predict dependence of energy deposition in the brain as a function of blast direction is somewhat surprising. However, since it has either been demonstrated or hypothesized in past work that brain damage is associated with shear loading [31] or cavitation [29, 30], our results suggest that these damage mechanisms will not be dependent on blast direction.

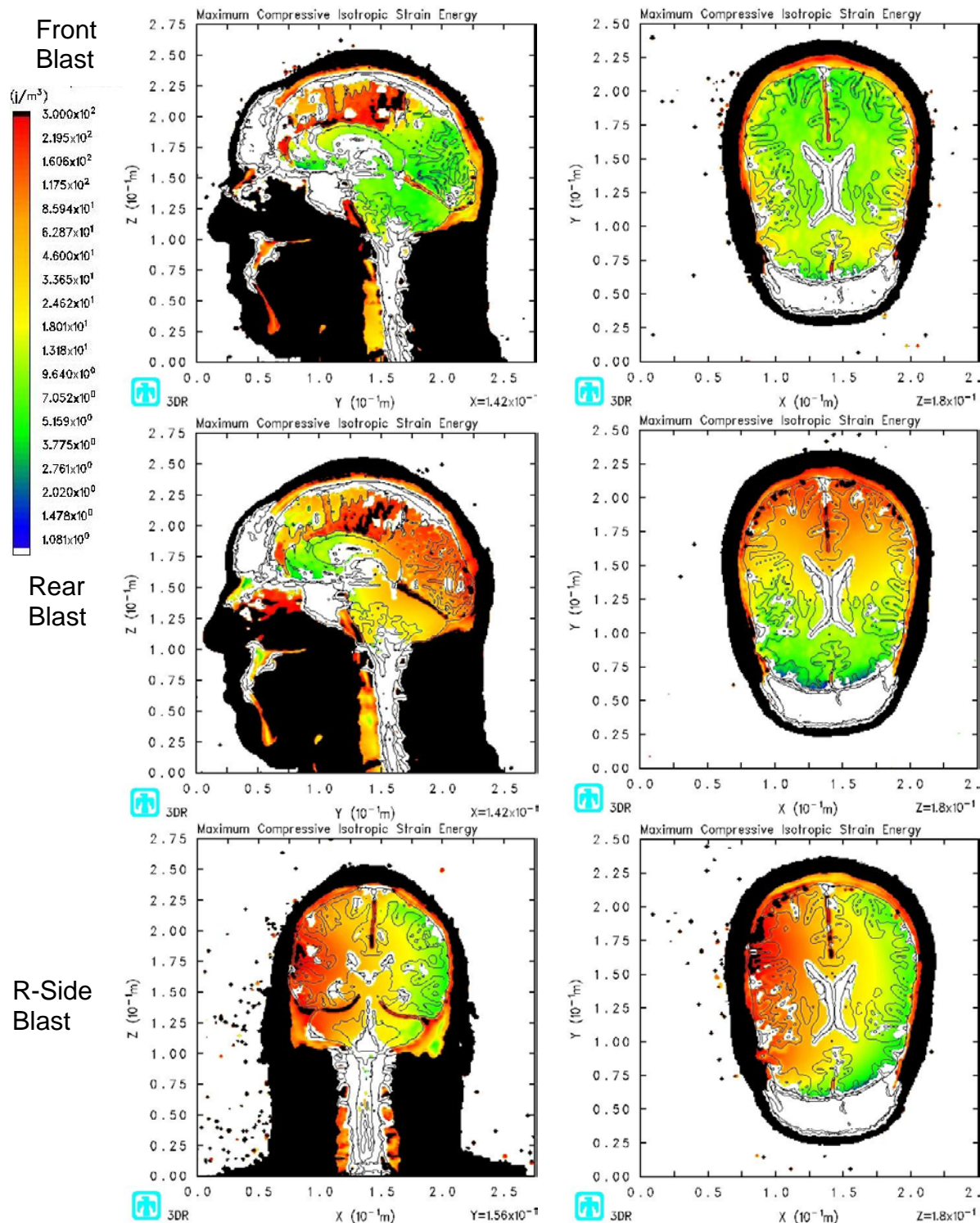


Figure 28. Plots of maximum Isotropic Compressive Energy in various anatomical planes for a 360 KPa blast. Top row: Frontal blast, mid-sagittal and axial planes; middle row: rear blast; bottom row: right side blast, mid-coronal and axial planes. Color scale: blue: 1  $J/m^3$ ; red: 300  $J/m^3$ , black denotes that the plot variable maximum limit has been exceeded. Positive energies are associated with compressive loading.

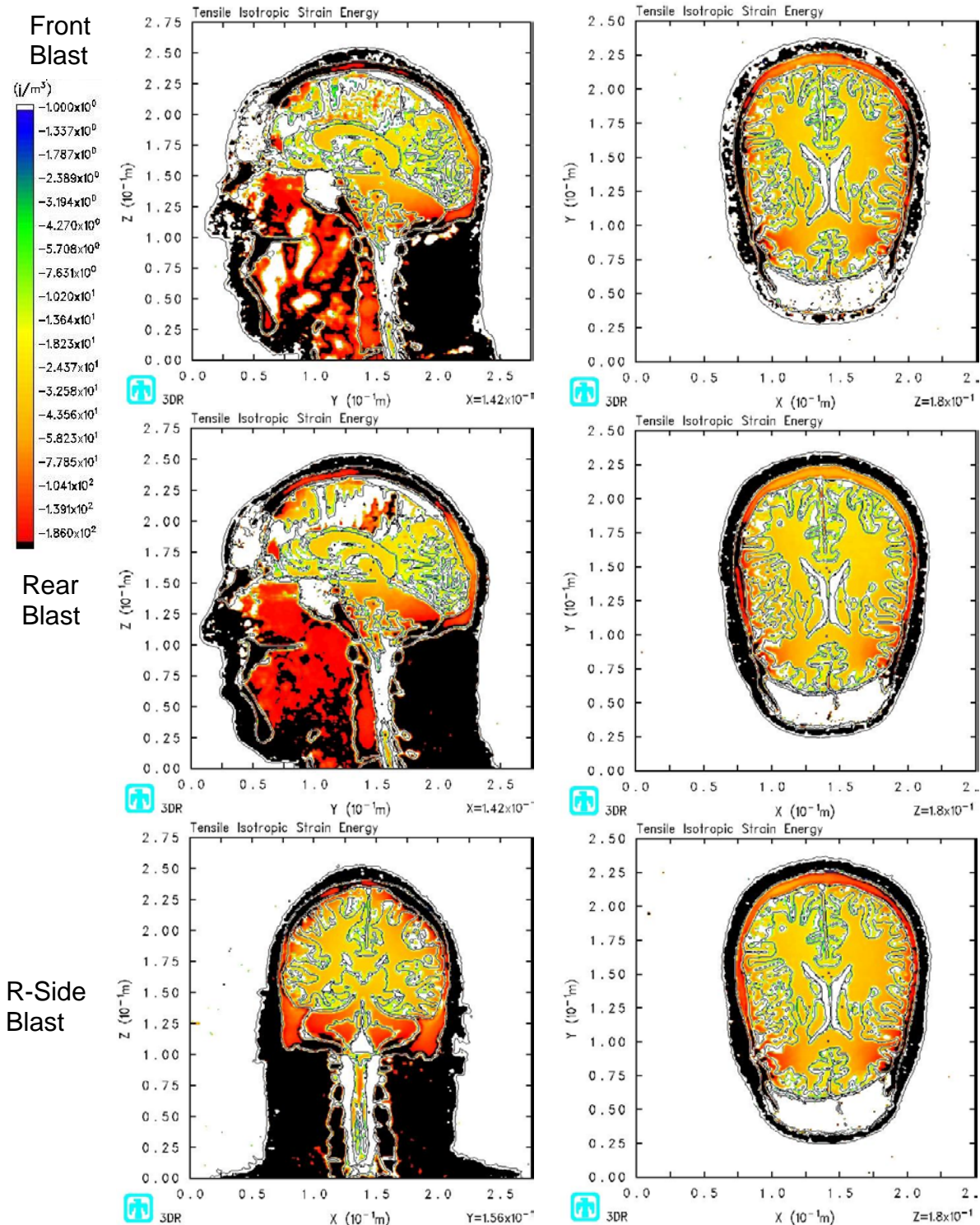


Figure 29. Plots of maximum Isotropic Tensile Energy in various anatomical planes for a 360 KPa blast. Top row: Frontal blast, mid-sagittal and axial planes; middle row: rear blast; bottom row: right side blast, mid-coronal and axial planes. Color scale: blue: 1 J/m<sup>3</sup>; red: 200 J/m<sup>3</sup>; black denotes that the plot variable maximum limit has been exceeded. Negative energies are associated with tensile loading.

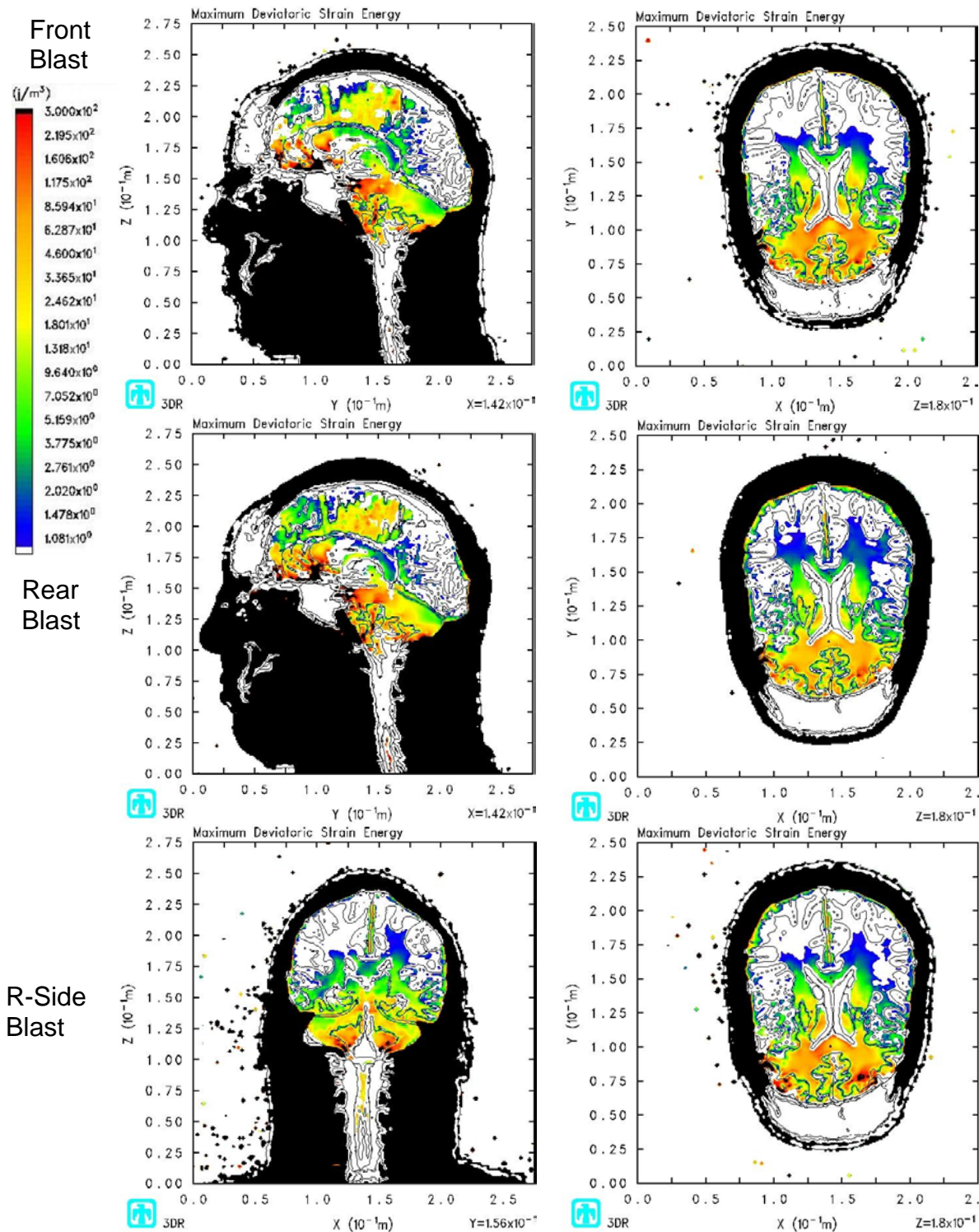


Figure 30. Plots of maximum Deviatoric (Shear) Energy in various anatomical planes for a 360 KPa blast. Top row: Frontal blast, mid-sagittal and axial planes; middle row: rear blast; bottom row: right side blast, mid-coronal and axial planes. Color scale: blue: 1 J/m<sup>3</sup>; red: 300 J/m<sup>3</sup>, black denotes that the plot variable maximum limit has been exceeded. Deviatoric energy is always positive.

### 4.3 Spatial Variance of Energy Deposition

The plots in Figure 28 suggest that a significant amount of isotropic compressive energy, associated with crushing, is deposited in the upper frontal region of the brain during frontal blast, in the occipital region for rear blast, and in the right temporal lobe for right-side blast. This is consistent with the coup-contre-coup hypothesis that assumes the brain regions closest to and farthest from the injury source (blast) will suffer the most damage. For example, in the frontal blast scenario, the coup site will be the frontal region of the brain whereas the contre-coup site is the occipital (rear) region. The opposite holds for rear blast in which the coup site is the occipital brain region and the frontal region will be the contre-coup site. As can be seen in the bottom row plots of Figure 28, the right temporal lobe is the coup site for the right-side blast scenario and the contre-coup site is the opposite (left side) temporal lobe.

Figure 29 suggests that the isotropic tensile energy, associated with dilatation, is higher in the outer cerebral regions, the upper brain stem, and in the cerebellum. This result is independent of blast direction and runs counter to the coup-contre-coup hypothesis. For each blast scenario, if we take into account the higher levels of compressive energy that occur at the coup site and the tensile energy deposition that also occur at that site, regardless of blast direction, we see that the brain tissue in that area can undergo a significant compression-to-dilatation swing in volume change. This volumetric swing may, in fact, lead to the cavitation process that has been hypothesized to occur in the brain under certain types of impulsive loading [29,30].

Figure 30 suggests that our simulations predict concentrated levels of deviatoric strain energy, associated with shearing and tearing, in the frontal brain region as well as the upper brain stem and cerebellum. As we have seen in Section 4.2, this outcome is independent of blast direction. If the work of Zhang et al. [31] is correct in its correlation of mild brain injury with shear stresses greater than 4-5 KPa in the thalamus, then our simulations predict that brain injury may in fact occur in the frontal region, upper brain stem, and cerebellum, for a blast of 360 KPa or greater, regardless of blast direction.

## 5 CONCLUDING REMARKS

This document is intended as a comprehensive progress report on our efforts to investigate blast-induced brain injury by means of a modeling and simulation approach as a basis to support analysis of traumatic brain injury, particularly from blast exposure.

Although we have been able to make significant progress in developing the M&S toolset and employing advanced clinical assessment methods, our success at collecting clinical data has been hampered by the scarcity of TBI subject volunteers for the project. As a result, we are unable to establish a quantitative correlation between simulation and clinical assessments of mTBI within the time constraints of the current project, which is scheduled to end in fall, 2012.

However, it has become apparent to us that with access to a larger TBI subject population, our clinical methods using various MR-based techniques and analyses shows great promise in identifying and mapping localized brain injury as a result of both blast loading and blunt impact to the head. In fact, this is the course we recommend for future work. That is, gain access to a larger TBI population ( $\geq 100$  subjects), conduct neuropsychological testing, magnetic resonance assessments (DTI and fMRI), apply independent component analyses (ICA) to identify and map brain regions displaying hypoactivity and hyperactivity, and attempt to correlate these results with various simulation predictions of the relevant injury scenarios. Once this correlation is established, we will then be in a position to develop a brain injury threshold criterion for blast exposure.

We feel that the body of work presented in this report clearly demonstrates the merit of using a modeling and simulation approach to investigate the intricacies of brain injury resulting from impulsive loading to the head and neck. Starting in fiscal year 2013, we will use laboratory directed research and development (LDRD) funds to extend this capability by developing a full head/neck/torso model and the related methodology to simulate the injury mechanics associated with blast loading, blunt force impact, and ballistic projectile penetration. This new M&S capability will allow us to investigate various armor strategies that mitigate injury to life-critical organs in the torso, neck, and head including the cardiovascular system, lungs, liver, spine, spinal cord, and brain. Once in place, we expect this capability to attract new partnership opportunities within the defense community who are interested in high fidelity investigations of wound ballistics and the development of advanced armor to protect our warfighters.

**INTENTIONALLY LEFT BLANK**

## REFERENCES

- [1] Centers for Disease Control and Prevention, 2007, “Traumatic brain injury in the US.”
- [2] Okie S., 2005, “Traumatic brain injury in the war zone,” *The New England Journal of Medicine*, **352**, pp. 2043–2047.
- [3] Defense and Veterans Brain Injury Center, “DoD Worldwide Numbers for TBI | DVVIC.”
- [4] Warden D., 2006, “Military TBI during the Iraq and Afghanistan wars,” *J. Head Trauma Rehabil.*, **21**, pp. 398–402.
- [5] Fischer H., 1991, U.S. military casualty statistics: operation New Dawn, operation Iraqi Freedom, and operation Enduring Freedom, Congressional Research Service.
- [6] DePalma R. G., Burris D. G., Champion H. R., and Hodgson M. J., 2005, “Blast injuries,” *N. Engl. J. Med.*, **352**(13), pp. 1335–1342.
- [7] Moore D. F., Radovitzky R. A., Shupenko L., Klinoff A., Jaffee M. S., and Rosen J. M., 2008, “Blast physics and central nervous system injury,” *Future Neurology*, **3**(3), pp. 243–250.
- [8] Taylor P. A., and Ford C. C., 2009, “Simulation of blast-induced early-time intracranial wave physics leading to traumatic brain injury,” *J. Biomech. Engr.*, **131**(6), p. 061007.
- [9] Moore D. F., Jérusalem A., Nyein M., Noels L., Jaffee M. S., and Radovitzky R. A., 2009, “Computational biology — modeling of primary blast effects on the central nervous system,” *NeuroImage*, **47**, **Supplement 2**, pp. T10–T20.
- [10] Moss W., King M., and Blackman E., 2009, “Skull flexure from blast waves: a mechanism for brain injury with implications for helmet design,” *Physical Review Letters*, **103**(10).
- [11] Gruzicic M., Bell W. C., Pandurangan B., and Glomski P. S., 2010, “Fluid/structure interaction computational investigation of blast-wave mitigation efficacy of the advanced combat helmet,” *Journal of Materials Engineering and Performance*, **20**(6), pp. 877–893.
- [12] Nyein M. K., Jason A. M., Yu L., Pita C. M., Joannopoulos J. D., Moore D. F., and Radovitzky R. A., 2010, “In silico investigation of intracranial blast mitigation with relevance to military traumatic brain injury,” *Proceedings of the National Academy of Sciences*, **107**(48), pp. 20703–20708.
- [13] 2007, “The National Library of Medicine’s visible human project.”
- [14] Zhang L., Yang K. H., and King A. I., 2001, “Comparison of brain responses between frontal and lateral impacts by finite element modeling,” *Journal of Neurotrauma*, **18**(1), pp. 21–30.
- [15] Carter D. R., 1984, *Biomechanics of bone*, Appleton & Lange.

- [16] Shuck L. Z., and Advani S. H., 1972, "Rheological response of human brain tissue in shear," *ASME J. Basic Engr.*, **94**, pp. 905–911.
- [17] Bayly P. V., Clayton E. H., Feng Y., Abney T. M., Namani R., Okamoto R. J., and Genin G. M., "Measurement of brain biomechanics in vivo by magnetic resonance imaging."
- [18] Feng Y., Abney T. M., Okamoto R. J., Pless R. B., Genin G. M., and Bayly P. V., 2010, "Relative brain displacement and deformation during constrained mild frontal head impact," *Journal of The Royal Society Interface*, **7**(53), pp. 1677–1688.
- [19] Hertel E. S., and Kerley G. I., 1998, *CTH reference manual: The equation of state package*, Sandia National Laboratories, Albuquerque, NM.
- [20] Nahum A. M., Smith R., and Ward C. C., 1977, "Intracranial pressure dynamics during head impact," *S.A.E. Proceedings of the 21st Stapp Car Crash Conference*, Warrendale, PA, pp. 339–366.
- [21] Merkle A., 2011, "Work in progress."
- [22] *Operator's care and use manual for the Lightweight Helmet (LWH)*, U.S. Marine Corps, Quantico, VA.
- [23] Hertel E. S., Bell R., Elrick M., Farnsworth A., Kerley G., McGlaun J., Petney S., Silling S., and Taylor P., 1993, "CTH: a software family for multi-dimensional shock physics analysis," *Proceedings of the 19th International Symposium on Shock Waves*, **1**, pp. 377–382.
- [24] *SIERRA Solid Mechanics Team*, 2011, *Sierra/SolidMechanics VOTD user's guide*, Engineering Sciences Center, Sandia National Laboratories, Albuquerque, NM.
- [25] Scherzinger W. M., and Hammerand D. C., 2007, *Constitutive models in LAME*, Sandia National Laboratories, Albuquerque, NM.
- [26] Swanson S. R., 1985, "A constitutive model for high elongation elastic materials," *Trans. ASME*, **107**, pp. 110–114.
- [27] Gruss E., 2006, "A correction for primary blast injury criteria," *J. Trauma-Inj. Infect. Crit. Care*, **60**(6), pp. 1284–1289.
- [28] Taylor P. A., Ludwigsen J. S., and Ford C. C., 2011, "Simulation of early-time intracranial wave physics leading to traumatic brain injury and its mitigation by various helmet designs for military personnel," *Proceedings of the 2011 Warheads and Ballistics Symposium*, Monterey, CA.
- [29] Brennen C. E., 2003, "Cavitation in biological and bioengineering contexts," *Proceedings of the 5th International Symposium on Cavitation*, Osaka, Japan.

- [30] Lubock P., and Goldsmith W., 1980, “Experimental cavitation studies in a model head-neck system,” *J. Biomech.*, **13**, pp. 1041–1052.
- [31] Zhang L., Yang K. H., and King A. I., 2004, “A proposed injury threshold for mild traumatic brain injury,” *Journal of Biomechanical Engineering*, **126**(2), p. 226.

**INTENTIONALLY LEFT BLANK**

## DISTRIBUTION

### External:

- 1 Office of Naval Research, Code 34  
Attn: Dr. Timothy Bentley (electronic copy)  
875 N. Randolph St.  
Arlington, VA 22203 P.O. Box 808, MS L-795  
[timothy.b.bentley@navy.mil](mailto:timothy.b.bentley@navy.mil)
- 1 The University of New Mexico  
Attn: Dr. Corey C. Ford (electronic copy)  
MSC10 5620  
1 University of New Mexico  
Albuquerque, NM 87131-0001  
[cford@salud.unm.edu](mailto:cford@salud.unm.edu)
- 1 Stanford University  
Attn: Dr. Andrei A. Vakhtin (electronic copy)  
Department of Psychiatry and Behavioral Sciences  
Main Administration  
401 Quarry Road  
Stanford, CA 94305-5717  
[avakhtin@stanford.edu](mailto:avakhtin@stanford.edu)
- 1 Washington University in Saint Louis  
Attn: Dr. Philip V. Bayly (electronic copy)  
Chair, Mechanical Engineering and Materials Science  
1 Brookings Drive  
St. Louis, MO 63130  
[pvb@wustl.edu](mailto:pvb@wustl.edu)

### Internal:

- |   |        |                     |                        |
|---|--------|---------------------|------------------------|
| 1 | MS1160 | Candice F. Cooper   | 5421 (electronic copy) |
| 1 | MS1160 | Douglas A. Dederman | 5421 (electronic copy) |
| 1 | MS1160 | Shivonne Haniff     | 5421 (electronic copy) |
| 1 | MS1160 | Chad B. Hovey       | 5421 (electronic copy) |
| 1 | MS1160 | Ryan J. Terpsma     | 5421 (electronic copy) |
| 1 | MS1160 | Kevin P. Ruggirello | 5421 (electronic copy) |
| 1 | MS1164 | Dennis R. Helmich   | 5420 (electronic copy) |
| 1 | MS0899 | Technical Library   | 9536 (electronic copy) |

**INTENTIONALLY LEFT BLANK**



**Sandia National Laboratories**